LIGHT SENSING PERFORMANCE OF AMORPHOUS SILICON THIN FILM PIN DIODES: STRUCTURE, INCIDENT LIGHT, AND PLASMA DEPOSITION EFFECTS

A Thesis

by

KAI PATRICK HENRY

Submitted to the Office of Graduate and Professional Studies of
Texas A&M University
in partial fulfillment of the requirements for the degree of

MASTER OF SCIENCE

Chair of Committee,	Yue Kuo
Committee Members,	Jorge M. Seminario
	Hung-Jen Wu
Head of Department,	Muhammad N. Karim

December 2016

Major Subject: Chemical Engineering

ABSTRACT

For hydrogenated amorphous silicon (a-Si:H) thin film PIN diodes fabricated using plasma-enhanced chemical vapor deposition, the effects of the n^+ layer deposition power, the existence of an aluminum reflector layer, and the incident light direction were investigated. Optical properties of photodiodes, e.g. open-circuit voltage, short-circuit current density, fill factor, efficiency, external quantum efficiency, series resistance, and shunt resistance, with respect to the aforementioned fabrication parameters, were investigated. Three monochromatic LED lights with different wavelengths, as well as a broad spectrum solar simulator, were used as the illumination sources in this research.

Plasma power influenced the n^+ film growth rate and resistivity, which affected the overall light detection efficiency in PIN diodes. The absorption of incident light was influenced by the band gap energies of the doped layers of a-Si:H and by the difference in mobility and lifetime of electrons and holes that were photogenerated in the intrinsic layer. The effect of device structure, fabrication conditions, light source, and incident light direction on the performance of a-Si:H PIN diodes was explored in this experimental study.

The growth rates and resistivities of doped a-Si:H thin films were found to correlate with the amount of RF power supplied during their deposition. The transmittance of *n*-type a-Si:H was also dependent on deposition power, and the effects varied depending on the wavelength of incident light exposure. Including a metallic reflector layer in the diode structure always improved its efficiency, especially for long

wavelength light, which is not effectively absorbed by a-Si:H. Generally, exposing the diodes to incident light on the *p*-side yielded better performance, due to the shorter required drift distance for photogenerated holes compared to *n*-side illumination.

DEDICATION

To all the friends I made who have made this journey so enjoyable. Sharing life's joys as well as its sorrows with you has made everything worth it.

To my high school chemistry teacher Mr. Tim Hoag. Your boundless enthusiasm for chemistry and learning has proved to be contagious! Without it I would not have embarked on my present journey of higher education.

To my family, who never left my side. I am eternally grateful for the love, learning, and fun that you all never ceased to provide.

And especially to my mom and dad, Kelly and Sean,

I love you forever.

ACKNOWLEDGEMENTS

I would like to thank my advisor, Dr. Yue Kuo, and my colleagues, Kibum Kim and Shumao Zhang, for their assistance and guidance in my work on this thesis and the research detailed therein. Thanks also to Texas A&M University for welcoming me into their community and providing an excelling environment for research and learning. Finally, I would like to thank the Electrochemical Society for the acceptance of my paper and the opportunity to present my research at the 229th ECS Meeting in San Diego, CA.

NOMENCLATURE

H	Hydrogen
B	Boron
P	Phosphorus
C	Carbon
Al	Aluminum
Si	Silicon
Ar	Argon
c-Si	Crystalline Silicon
a-Si	Amorphous Silicon
a-Si:H	Hydrogenated Amorphous Silicon
ITO	Indium Tin Oxide
RF	Radio-frequency
PECVD	Plasma-enhanced Chemical Vapor Deposition
I	Current
J	Current Density
V	Voltage
I_{SC}	Short-circuit Current
J_{SC}	Short-circuit Current Density
V_{OC}	Open-circuit Voltage
FF	Fill Factor

η	Efficiency	
EQE	External Quantum Efficiency	
R_S	Series Resistance	
R_{SH}	Shunt Resistance	
λ	Wavelength	
v	Frequency	
q	Elementary Charge	$= -1.602 \times 10^{-19}$ C
h	Planck's Constant	$= 6.626 \times 10^{-34}$ J s
c	The Speed of Light	$= 3.00 \times 10^{8}$ m s^{-1}
k	Boltzmann Constant	$= 1.38 \times 10^{-23}$ J K^{-1}

TABLE OF CONTENTS

Page

LIST OF FIGURES

FIGURE Page

FIGURE Page

LIST OF TABLES

1. INTRODUCTION

1.1. The Photovoltaic Effect and Semiconductors

The photoelectric effect, which was described on a physical level by Albert Einstein in 1905 [1], is the process by which electrons are ejected from a material through the absorption of incident light. The photovoltaic effect is a specific application of the photoelectric effect. While the latter describes electrons ejected from a substance via photon energy, the former refers to electrons that are energized, but still remain in the material. In materials that undergo the photovoltaic effect, charge carriers exist in two, distinct "energy bands" as shown in Figure 1.1. Electrons in their ground state are found at or near the valance band. Here, they are bound to their specific nucleus and are thus not useful for conducting a current. In the photovoltaic effect, an electron may absorb the energy from an incoming photon and rise to the conduction band. At this elevated energy state, electrons are free to travel among neighboring atoms and are therefore able to conduct a current. It is also sometimes useful to think of holes as an effective charge carrier defined by the absence of an electron. In this case, holes absorb the energy of a photon and are "lowered" from their ground state in the conduction band to the valence band where they may conduct current in the opposite direction of electron flow.

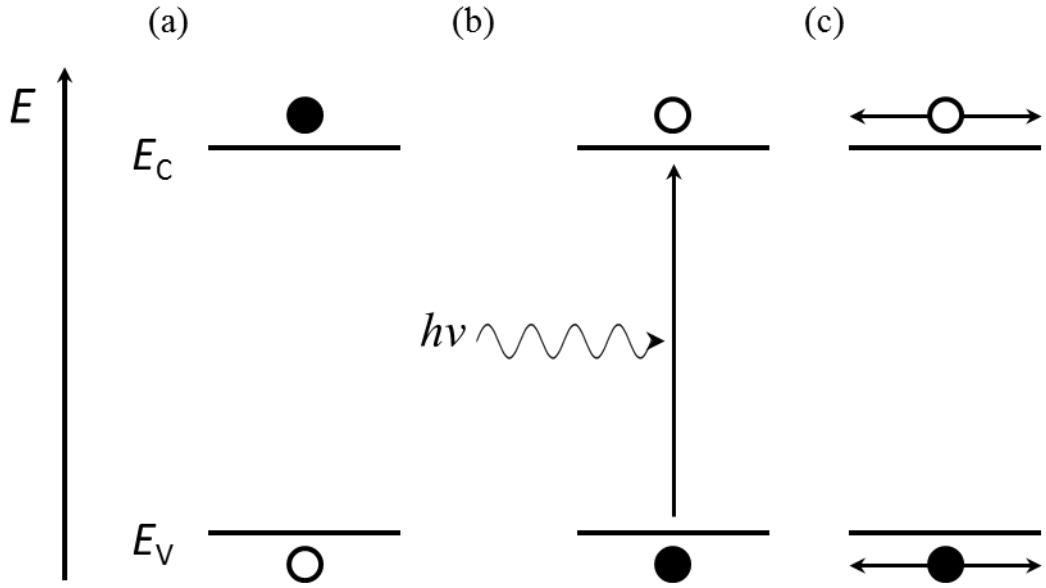

Figure 1.1: Energy band diagram of the photovoltaic effect. The vertical axis represents the energy level of a charge carrier. (a) At their respective ground states, electrons (white circles) occupy the valence band and holes (black circles) occupy the conduction band. (b) By absorbing the energy of a photon, an electron in the valence band may exchange places with a hole in the conduction band. (c) An electron in the conduction band can conduct a negatively charged current and a hole in the valence band can conduct a positively charged current.

The first successful demonstration of the photovoltaic effect was performed by Alexandre-Edmond Becquerel in 1839 [2]. At the age of 19, Becquerel discovered light-induced generation of electricity when he exposed two electrodes of conductive metals such as gold or platinum to light in the ionic solution of an electrochemical cell [3]. Since then, spurred by the continual discovery of semiconductor materials (including but not limited to selenium, silicon, and cadmium sulfide), the photovoltaic effect has been utilized in solid state devices for the generation of electricity.

At a time when renewable energy is steadily growing in prominence and adoption, there may come a moment when photovoltaics begin to significantly

outcompete against nonrenewable sources of energy in terms of cost efficiency. Nations such as Germany are presently enacting sweeping additions of solar power to their power grid. Photovoltaics accounted for 6.4% of Germany's gross electricity consumption in 2015 [4], and renewable energy accounted for 30% of gross electricity consumption in 2014 [5]. Today, solar panels are integrated into buildings, automobiles, and handheld devices as primary or auxiliary means of supplying them with power. Modern solar cells are possible due to the discovery and proliferation of semiconductor materials.

Semiconductors are one of three main categories of materials that differ based on their electrical properties—the other two being conductors and insulators. Specifically, these materials differ by the magnitude of their band gap energy. The band gap is defined as the difference in energy between the conduction band (E_C) and the valence band (E_V) (see Fig. 1.1). In conductors, this difference, $E_C - E_V = E_g$, is miniscule or non-existent; electrons in their ground state readily occupy the conduction band and are able to conduct a current. In insulators, E_g is very large (e.g. > 5 eV), so charge carriers in these materials are generally unable to conduct a current. In semiconductors, E_g is small but nonzero (generally between 0.3 and 3 eV) [6]. Thus, while semiconductors act as insulators in their ground state, they may be tuned to act as conductors via altered material properties due to outside stimuli.

The most commonly used semiconductor material is silicon. It was first classified as an element bearing its present name by Thomas Thomson in 1817 [7], and Jöns Jacob Berzelius is credited with the discovery of Si in its pure form in 1823 [8]. Pure Si first

existed as amorphous silicon (a-Si), but Si in its crystalline form (c-Si) was the first to be used for transistor devices.

A diode is a type of electrical device that conducts a current in one direction of ("forward") but is resistive in the other ("reverse") direction. The functionality of a diode is reliant on material properties of semiconductor materials, since conductors would indiscriminately conduct in either direction and insulators would not conduct a current at all. A photodiode is a specific type of diode that uses incident light to generate the photovoltaic effect to create useful charge carriers in the semiconductor. In order to achieve the one-way conductivity, semiconductor materials are doped—that is, impurities are substitutionally inserted into the semiconductor layer. *N*-type doped semiconductors have excess electrons and *p*-type doped semiconductors have a deficit of electrons or an excess of holes. Doping is typically performed *in situ* during the fabrication of the semiconductor device [9].

1.2. The *p*-*n* Junction

Diodes made of semiconductors often have a *p*-*n* junction structure, shown in Figure 1.2, which results in an intrinsic voltage, V_{bi}, between the *p*- and *n*-type regions. This voltage creates a depletion region which is an insulating barrier that results from holes diffusing out of the *p*-type region toward the *n*-type region, and electrons diffusing out of the *n*-type region toward the *p*-type region. When a voltage is applied in the same direction as V_{bi} ("reverse bias," Fig. 1.2(b)), the depletion region widens and current is restricted. When a voltage is applied in the opposite direction of V_{bi} ("forward bias," Fig. 1.2(c)), the depletion region narrows and the flow of charge carriers across the

junction is enhanced. At a high enough forward bias, the depletion region completely disappears and excitons movement is only due to applied voltage. In a *p*-*n* diode, power is *generated* when a forward voltage bias is applied that is less than V_{bi} such that the net voltage is still in the reverse direction. Power is *consumed* when a reverse voltage bias is applied or if a forward bias is applied that exceeds the magnitude of V_{bi}. In Si, boron (B) and phosphorus (P) are the most common elements used for *p*- and *n*-type doping, respectively. B and P contain one fewer and one more valence electron compared to Si, respectively, which contributes to the excess of majority charge carriers in the material. These charge carriers readily recombine at the depletion region of the *p*-*n* junction. In the case of photodiodes such as solar cells, incident light imparts energy to these charge carriers which increases the magnitude of the current within the material.

Solar cells are typically made of c-Si which is comprised of an orderly lattice structure and few defects. It allows for the uninterrupted flow of charge carriers with minimal chances of recombination during diode operation. For this reason, the efficiency of c-Si solar cells is highly dependent on the quality and crystallinity of the Si [10].

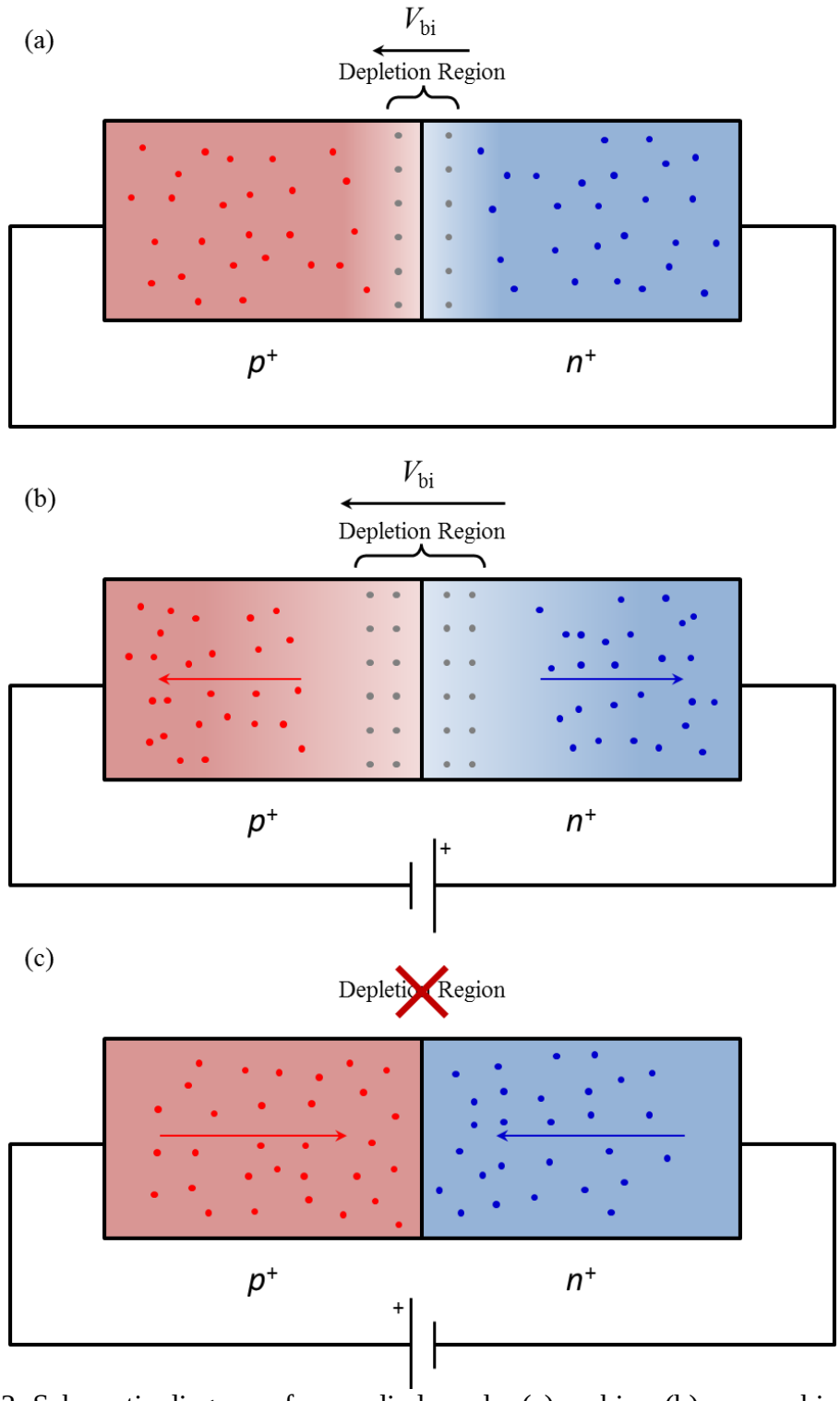

Figure 1.2: Schematic diagram of a *p*-*n* diode under (a) no bias, (b) reverse bias, and (c) forward bias. Electrons and holes are indicated by blue and red dots, respectively. Gray dots indicate excitons that have recombined in oppositely charged regions.

1.3. Amorphous Silicon

An alternative material to c-Si is a-Si. Despite a-Si being discovered first, it was not until over a hundred years later that high throughput fabrication methods for a-Si:H films were developed by Chittick et al. in 1969 [11]. However, intrinsic a-Si:H was not useful for the production of diodes or transistors because its high defect density prevented the effective doping of the material [12]. In 1975 Spear & Le Comber demonstrated that a-Si:H films could be prepared into *p*- and *n*-type semiconductor materials by introducing B_2H_6 and PH_3 gases, respectively, during the glow discharge deposition process [12]. This landmark paper paved the way for the use of amorphous solids for applications in optical and electronic devices.

A-Si differs from c-Si in that the former is comprised of a disordered network of Si. Figure 1.3 shows the atomic structures of c-Si and a-Si:H. (In order to passivate dangling bonds that necessarily arise from the disordered structure of a-Si, hydrogen (H) is often introduced to form a-Si:H.) Like carbon (C), Si contains four valence electrons and readily forms four bonds with neighboring atoms. C-Si has a diamond tetragonal lattice with a lattice parameter, *a*, of 5.43 Å, while a-Si:H has a "glassy" non-crystalline structure. Although a-Si:H has a more random structure, the average bond length between neighboring Si atoms in a-Si:H does not differ much from that of c-Si [13]. A-Si:H has become widely used in the fabrication of transistors and diodes due to its simple fabrication process and relatively low raw material requirement [14] [15] [16]. A-Si:H thin films can be fabricated with thicknesses on the order of 200 nm and maintain full diode functionality.

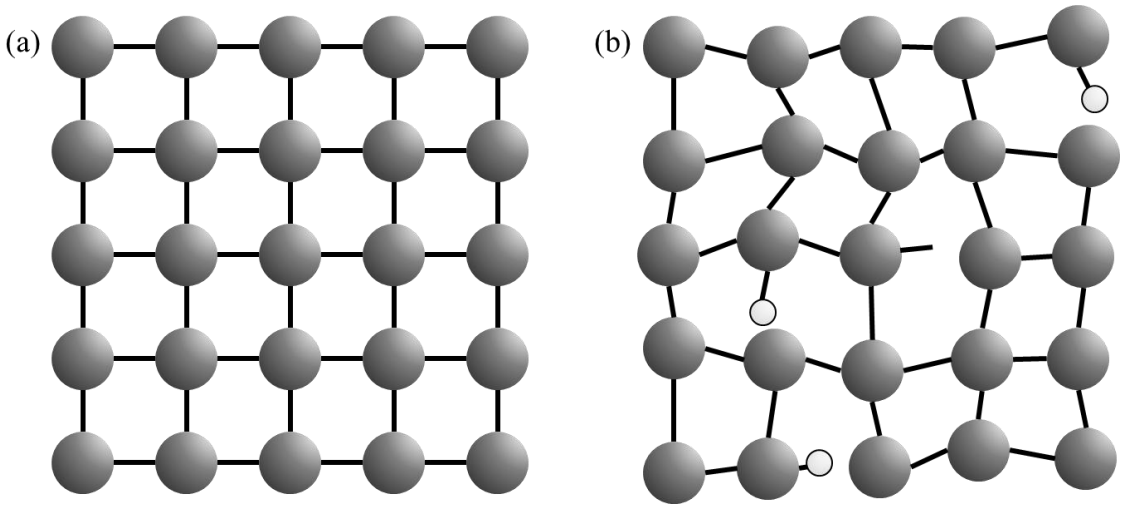

Figure 1.3: Lattice structure of (a) c-Si and (b) a-Si:H. In perfectly crystalline Si, all Si atoms are tetrahedrally bonded to four neighboring Si atoms. However, in a-Si:H, some Si-Si bonds may be broken. The introduction of H atoms (white spheres) helps to passivate the dangling bonds that are otherwise present in a-Si:H.

Therefore, although devices made from a-Si:H have worse performance than those made of c-Si [17], a-Si:H is still a common material used in solar cells, thin film transistors, optical sensors, and other electronic devices [6].

There is one characteristic, however, of a-Si:H that must be taken into account when it is used in the production of thin film diodes. When dopants are introduced into the network of a-Si:H, they necessarily introduce defects into the structure which manifest as dangling bonds (see Fig. 1.3) [18]. These dangling bonds act as charge trapping sites which greatly reduces the current flow in the diode. The function of diodes is reliant on the mobility of minority charge carriers: electrons in *p*-doped regions or holes in *n*-doped regions. If the defect density of the doped material is high, minority charge carriers will recombine at defect sites before they are able to travel through the

circuit [19]. Thus, when using a-Si:H in the fabrication of diodes, the PIN structure must be used instead of the *p*-*n* structure.

1.4. The PIN Diode

The PIN diode, shown in Figure 1.4, is another doping structure of semiconductor materials. The main difference between *p*-*n* and PIN diodes is that in the latter, an additional intrinsic (*i*) semiconductor layer is inserted between the *p* and *n* layers. This is because, compared to doped a-Si:H, intrinsic a-Si:H contains far fewer defects and dangling bonds [20]. The PIN structure allows charge carriers to travel a greater distance within the diode before encountering a scattering or recombination event. Thus, when PIN photodiodes are exposed to incident light, most of the excitons are generated in the *i* layer. These excitons then travel in the direction dictated by the direction of the applied voltage as well as the internal electric field from the *p*- and *n*-type layers. Note that, due to the vertically stacked layer structure, incoming photons must travel through the doped a-Si:H layers in order to reach the intrinsic layer. Therefore, in order to maximize diode performance, ideally one would minimize the amount of light absorption in the doped layers. This can be accomplished in two ways. First, the doped layers are kept as thin as possible while still generating a built-in electric field within the diode. In conventional a-Si:H PIN thin film solar cells, the thicknesses of the *p*- and *n*-type layers are on the order of 10 nm, whereas the *i* layer thickness is in the range of 150-300 nm. Second, the window layer—that is, the first layer to be exposed to incident light, which is generally the *p* layer—is alloyed with other materials.

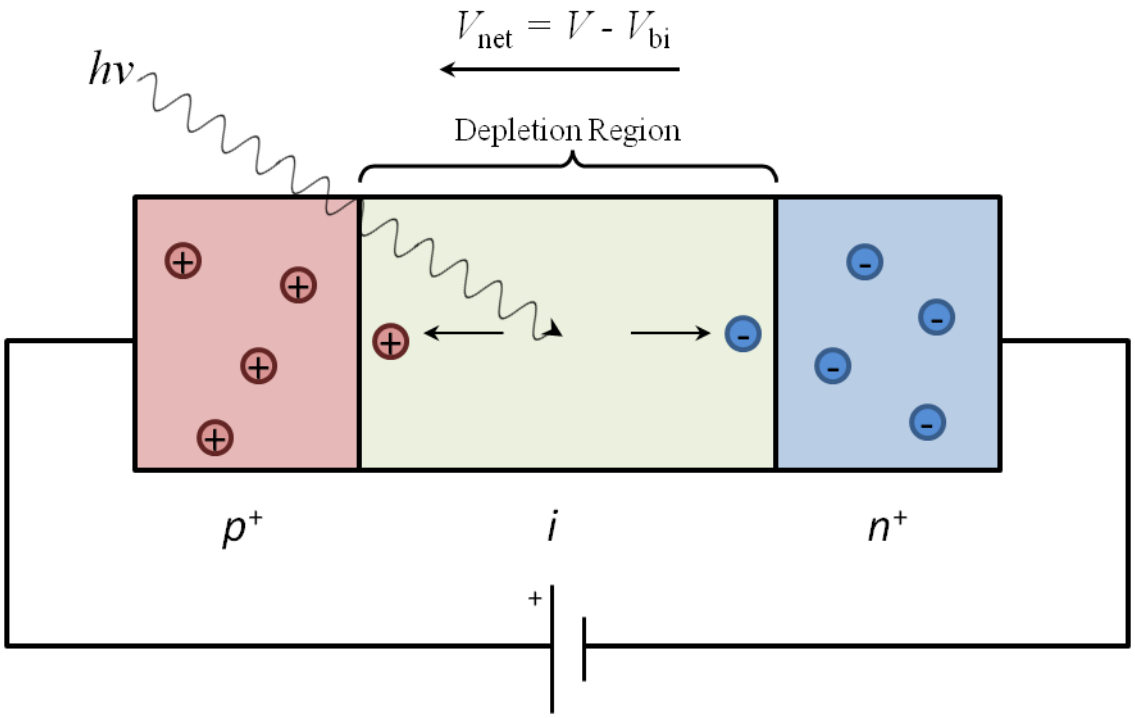

Figure 1.4: Schematic diagram of a PIN diode under illumination and applied forward (net reverse) bias.

Since *p*-type a-Si:H possesses a higher optical band gap than *i*- or *n*-type a-Si:H, therefore it does not effectively absorb low energy photons (<1.9 eV). By alloying a-Si:H with materials such as C, producing amorphous hydrogenated silicon carbide (a-SiC:H), the band gap is further widened. The amount of incoming photons that can be absorbed by the *p* layer is reduced, allowing more of them to reach the *i* layer. [20]. However, the introduction of C complicates the deposition process. Therefore, in this work, only B and P were used as additives in the a-Si:H diodes fabricated in this study.

1.5. Plasma-enhanced Chemical Vapor Deposition

Work performed by Chittick, et al. [11] and Spear & Le Comber [12] demonstrated some of the earliest documented means of fabricating a-Si:H thin films

using the glow discharge method in a PECVD system. This particular method allows for the deposition of wide area a-Si:H films using SiH_4 gas as a precursor and B_2H_6 or PH_3 as the doping gas. Other gases, such as H_2, Ar, and N_2, can be included in the feed gas stream to improve the film quality and uniformity [21] [22].

1.5.1. Mechanism of Action

PECVD processes begin with the placement of a substrate into a strong vacuum environment (e.g. on the order of 100-1000 mTorr). Once the PECVD chamber is evacuated, the precursor gases are introduced. By themselves, these gases do not chemically react with the substrate, therefore they do not deposit. Contained within the PECVD chamber are two parallel plate electrodes. When supplied with radio frequency (RF) power, these electrodes ionize the precursor gases and also create a downward electric field. Thus, not only do the precursor gases become positively charged radicals, but they are also directed to impact onto the substrate surface, where they then react and form the desired thin films.

1.5.2. Experimental Setup

The PECVD system used for this research is an AMP-3300 series PLASMA I reactor system made by Applied Materials, and a schematic diagram of the apparatus structure is shown in Figure 1.5. The chamber contains two parallel-plate electrodes separated by 5 cm. The top electrode (also simply called the electrode) is 72 cm in diameter and is driven by a 50 kHz RF generator. The bottom electrode (also called the platen) is grounded and is also 72 cm in diameter. At the center of the platen is a 2 cm diameter grated hole through which the feed gases are introduced. Exhaust species then

exit out through ports at the edge of the chamber beneath the platen. The substrate is placed on the platen which can be heated to facilitate plasma formation.

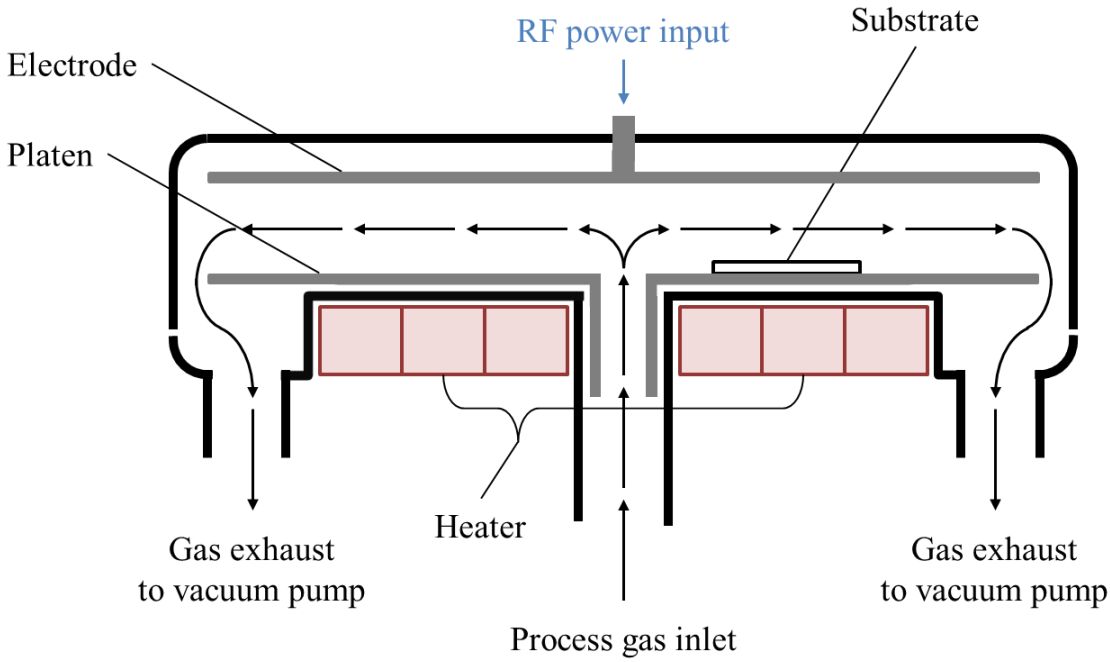

Figure 1.5: Schematic diagram of the PECVD reactor.

1.6. Characterization of PIN Diodes Under Light Illumination

To characterize the performance of a-Si:H PIN diodes, one can apply a bias voltage, sweeping from negative to positive voltages (see Fig. 1.2), and measure the current generated within the diode. This procedure is repeated under various illumination conditions to determine the diode's current-voltage (*I-V*) or current density-voltage (*J-V*) characteristics. Figure 1.6 shows an *I-V* curve for a typical a-Si:H PIN diode operated under illumination.

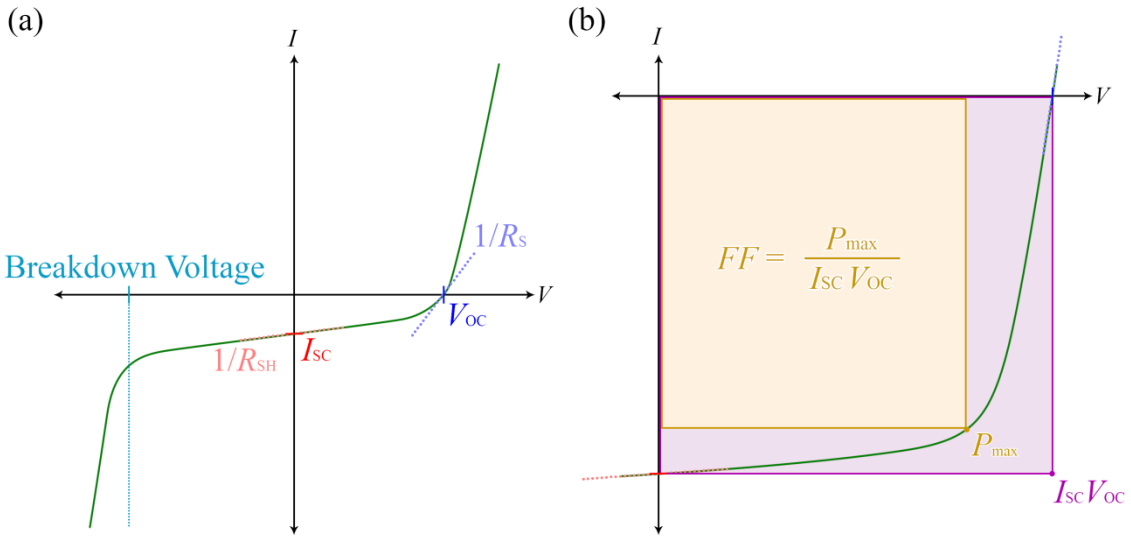

Figure 1.6: Idealized current-voltage curve for a PIN photodiode under illumination. Figure (a) shows the entire region of examined voltages, and Figure (b) focuses on the fourth quadrant, where the diode exhibits photovoltaic behavior and power generation.

From this curve, one can calculate several properties of the cell, including short-circuit current (I_{SC}), open-circuit voltage (V_{OC}), fill factor (FF), efficiency (η), external quantum efficiency (EQE), series resistance (R_S), and shunt resistance (R_{SH}).

1.6.1. Equivalent Circuit

The solar cell, as a photodiode, can be thought of as an electrical device with an equivalent circuit to Figure 1.7. Incoming light generates the photocurrent (J_{ph}) within the diode with net voltage (V in Fig. 1.7). Some current is lost immediately due to recombination losses (J_{rec}) while the remaining charge carriers travel through the diode medium. There are two primary sources of resistance losses in a Si diode, R_S and R_{SH}, which are detailed in sections 1.6.7 and 1.6.8, respectively. One additional source of

resistance is within the applied load itself (R_L) though this is not detectable in the *J-V* curve.

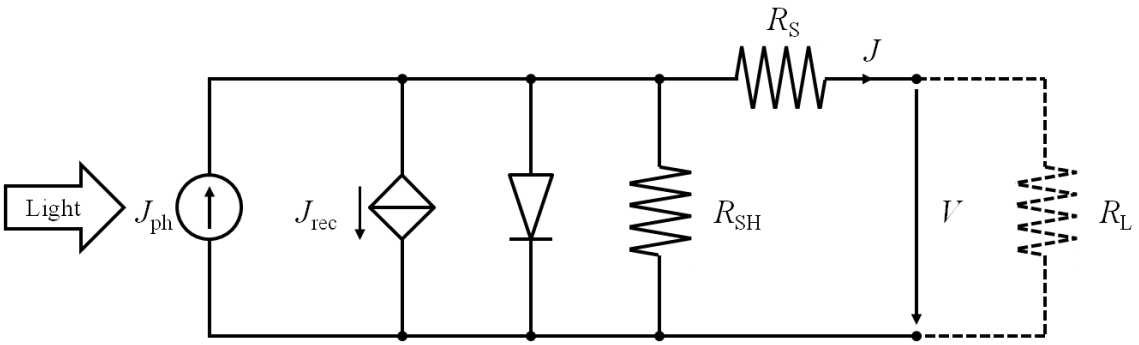

Figure 1.7: Equivalent circuit diagram for a real solar cell. Note that *V* in this figure refers to the *net* voltage in the solar cell, equal to the difference between bias voltage (*V* in Fig. 1.6) and built-in voltage (V_{bi}).

1.6.2. Short-circuit Current (Density)

The short-circuit current (I_{SC}) is the amount of electron flow in a diode when no external voltage is applied (see Fig. 1.6(a)) [20]. Often, current density (*J*), which is the total current divided by the active area of the diode, is used instead of current as it simplifies calculations when taking into account incident light intensity. Under illumination, the short-circuit current density (J_{SC}) of an ideal diode is solely dependent on the incoming photon flux. Figure 1.8 shows the dependence of J_{SC} on the E_g of the diode material. This simple relationship shows that, as the semiconductor band gap increases, the J_{SC} of the material decreases. This is because, at higher values of E_g, fewer incident photons will have sufficient energy to overcome this gap. Photons with low energy do not generate useful excitons in the diode, and only result in thermal re-emission from the cell. For optimal solar cell performance, larger values of J_{SC} are

generally better, and it is indicative of more available power to be generated from the cell.

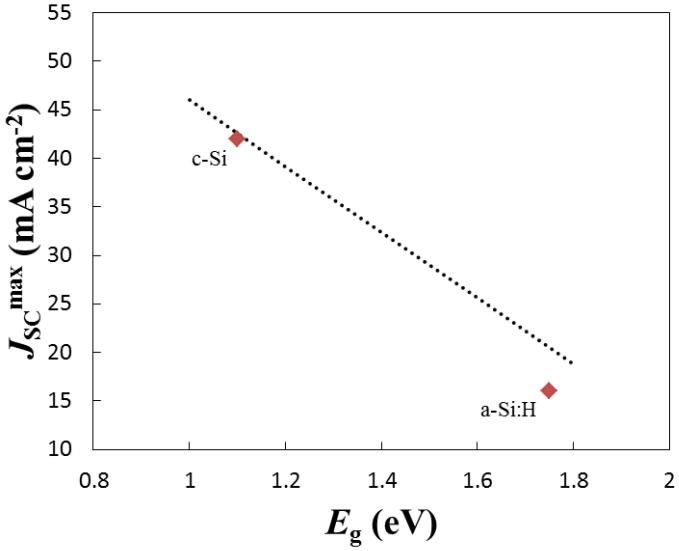

Figure 1.8: Theoretical maximum value of open-circuit density vs. band gap energy for different types of Si photodiodes. Reference values of J_{SC}^{max} from Shah [20].

1.6.3. Open-circuit Voltage

The open-circuit voltage (V_{OC}) of a photodiode is the value of applied voltage bias (V) where I or $J = 0$ (see Fig. 1.6(a)) [20]. For PIN diodes, V_{OC} is roughly dependent on the magnitude of V_{bi}. Recall from § 1.4 that *p*-*n* and PIN junctions possess an intrinsic voltage, V_{bi}, due to the uneven distribution of charge carriers in the doped regions of the diode. Thus, for the internal current within the diode to be zero, V must roughly be equal in magnitude to V_{bi}. Note that V_{bi} is dictated by following equation:

$$V \tag{1.1}$$

where E_{int} is the internal electric field of the diode due to doping and d_i is the thickness of the intrinsic layer of the PIN diode. This is simply the relationship between voltage and a uniform electric field. If the charge density of the *i* layer is assumed to be zero, then E_{int} is roughly constant and V_{bi} therefore depends only on the thickness of the *i* layer. As a consequence, if the *i* layer is too thin, the value of V_{bi} will be small, resulting in little available power in the diode. For optimal solar cells, larger values of V_{OC} are better, as they are indicative of more available power to be generated from the cell. During operation, solar cells only generate power when the applied voltage V is positive but less than V_{bi}. If V is negative, charge carriers travel along the built-in potential and no power is generated. If V is positive but exceeds V_{bi}, the internal electric field is overpowered and charge carriers move in the opposing direction.

For the characterization of diodes, J_{SC} and V_{OC} are generally the only values that are directly measured. The remaining properties that follow are all calculations based on data acquired from the diode's *J*-*V* curve.

1.6.4. Fill Factor

The fill factor (*FF*) of a solar cell is the first of several means of quantifying the cell's performance. It is a dimensionless metric, and is a graphical representation of the ratio between the peak power generated within the diode (P_{max}) and the area enclosed by the rectangle indicated by $I_{SC}V_{OC}$ (see Fig. 1.6(b)):

$$FF = \frac{P_{max}}{I_{SC}V_{OC}} \tag{1.2}$$

Equivalently, in terms of surface power density (P_d) and current density, *FF* can be represented as:

(1.3)

Higher values of *FF* indicate better diode performance. In optimized a-Si:H solar cells, typical values of *FF* are between 0.65 and 0.75 [20].

1.6.5. Efficiency

The efficiency or conversion efficiency (η) of a solar cell is defined by the following equation:

(1.4)

where $P_{d,max}$ is the peak surface power density in the cell and E_e is the irradiance (or radiant flux) incident on the cell [23]. Both terms have units of W m^{-2}. Equivalently, using the definition of *FF* in Eq. 1.4, η can also be written as:

(1.5)

In other words, the efficiency of a solar cell is the ratio between the peak power within the cell and the power of the incident light.

There are multiple ways to quantify solar cell efficiency, but when most refer to the "efficiency" of a solar cell in commercial contexts, they are referring to η. According to Richter, et al., the theoretical maximum efficiency of a c-Si solar cell is 29.43% [24]. At the time of this writing, SunPower has achieved an efficiency of 24.2% in full scale solar cells, confirmed by the U.S. Department of Energy's NREL [25]. According to

Carlson & Wronski, the theoretical maximum efficiency of a-Si solar cells is estimated to be 14-15% [26]. At the time of this writing, Kabir et al. has achieved a maximum efficiency of 10.02% (prior to stabilization) in single-junction a-Si solar cells [27].

1.6.6. External Quantum Efficiency

In contrast to η, the external quantum efficiency (*EQE*) of a photodiode is defined by the ratio between collected electron-hole pairs and incident photons [20]:

$$EQE = \frac{|J_{SC}/q|}{E_e/\left(\frac{hc}{\lambda}\right)} \tag{1.6}$$

The numerator term is the short-circuit density divided by the elementary charge of an electron and the denominator term is the irradiance of the incident light divided by the energy of a photon. Thus, like η, *EQE* is a dimensionless parameter. Note that Eq. 1.6 is only useful when describing solar cells illuminated by a single wavelength of light, indicated by the λ term. To calculate *EQE* for broad spectra, such as sunlight, one instead employs the following equation:

$$EQE = \frac{|J_{SC}/q|}{\sum_{\lambda} E_{e,\lambda}\Delta\lambda/hc} \tag{1.7}$$

Here, the denominator term is the Riemann sum of spectral irradiances, $E_{e,\lambda}$ (with dimensions of W m^{-2} nm^{-1}), over the energies of photons of all partial wavelengths, $\Delta\lambda$, of incident light. For laboratory purposes, *EQE* is often considered a more useful measurement than η since the former more directly accounts for the physics of the solar cell. Compared to the theoretical limitations of η, *EQE* can reach values near unity (one exciton created for every incident photon) or, in some cases such as under particularly

high energy light, greater than unity (wherein a single photon may occasionally generate multiple excitons in a solar cell) [28]. In the research conducted in this thesis, *EQE* was used as the primary parameter for characterizing the performance of the devices fabricated therein.

1.6.7. Series Resistance

When a current is conducted through a medium, the current will experience a resistance governed by Ohm's law:

$$-\qquad (1.8)$$

Based on the graphical representation of *I-V* curves (see Fig. 1.6), Eq. 1.8 can be represented approximately as the inverse of the slope of the *I-V* curve:

$$—\qquad (1.9)$$

When a solar cell is operated at open-circuit, the applied voltage cancels out the built-in voltage in the diode and the net current is zero. It is under this operation mode that R_S is the dominant form of measurable resistance within the diode, and it is the resistance that charge carriers experience when traveling through the full circuit and diode medium. R_S is to be minimized for optimal solar cell operation.

1.6.8. Shunt Resistance

When no bias voltage is applied to the solar cell, only V_{bi} remains. During this mode of operation, R_{SH} is the dominant form of measurable resistance within the diode. This resistance occurs when charge carriers bypass the circuit and shunt through the diode. R_{SH} is to be maximized for optimal solar cell operation.

1.7. Summary

In the preceding introduction, the physics of solar cell and general diode operation has been discussed. The role of the photovoltaic effect was explained in the basic function of solar cells, and the history of its discovery as well as its effect on the science of electronic devices was shown.

It was explained that diodes can take on a number of forms, including *p-n* and PIN configurations. Solar cells can be fabricated with several different types of semiconducting materials, and even silicon can take on different morphological phases, including c-Si and a-Si:H. For the purposes of the research conducted in this thesis, all diodes were fabricated using a-Si:H in a PIN configuration. PECVD was the primary method used to fabricate these devices, and it was chosen due the ease with which it can introduce dopants *in situ* during the deposition of the Si.

Finally, it was shown how the performance of solar cells is characterized. For the purposes of this research, J_{SC}, V_{OC}, FF, η, EQE, R_S, and R_{SH} were the metrics that were used. With this background in place, the remainder of this thesis elaborates on the experiments that were performed in pursuit of the research goals.

2. EXPERIMENT 1: GROWTH RATE AND RESISTIVITY OF a-Si:H

The following experiments described within this thesis were intended to correlate the performance of a-Si:H thin film solar cells to the process parameters used during the PECVD fabrication of the cells. This section contains portions adapted from a paper submitted in May 2016 by K. Henry and Y. Kuo [29], reproduced by permission of The Electrochemical Society.

2.1. Motivation

There are several parameters that can be varied during the PECVD fabrication of a-Si:H thin films including RF power or frequency, chamber pressure, temperature, and process gas flow rate. For the deposition of the thin films in this research, it was decided that the single parameter to be altered was the RF power (or deposition power) supplied during the deposition of the n^+ layer in the PIN diode. The effect of varying deposition power on the light sensing ability of PIN diodes has been studied in the past [30]. However, the influence of RF power supplied specifically during the deposition of the P-doped n^+ layer is not well understood. It is difficult to predict the doping incorporation or the doping efficiency in the n^+ layer when varying RF power, and most conclusions are based on empirical results [19] [31]. For the first experiment, the effect of RF power on the deposition rate and resistivity of doped a-Si:H thin films was investigated. Using these data, subsequent devices with the n^+ layer deposited at different power could be fabricated with fixed thicknesses. Depositions were performed for *p*-type films as well, but only *n*-type film deposition conditions were varied for subsequent experiments.

2.2. Experimental

2.2.1. Growth Rate

Using PECVD, *p*- and *n*-type a-Si:H thin films were deposited directly onto Corning 1737 glass substrates, varying only the RF power, for a total of eight different conditions which are listed in Table 2.1.

Table 2.1: Deposition conditions of doped a-Si:H thin films.

	Gas Flow Rate (sccm)				Power	Pressure	Deposition Time
Sample	**SiH_4**	**H_2**	**B_2H_6 (2% in H_2)**	**PH_3 (7% in H_2)**	**(W)**	**(mTorr)**	**(min)**
1	60	1000	-	20	200	700	30
2	60	1000	-	20	300	700	30
3	60	1000	-	20	400	700	15
4	60	1000	-	20	500	700	15
5	35	400	20	-	150	700	30
6	35	400	20	-	200	700	15
7	35	400	20	-	300	700	15
8	35	400	20	-	400	700	15

Once the films were prepared, each of their thicknesses was measured using a Dektak profilometer. These thicknesses were then divided by their respective deposition time to obtain the growth rate for doped a-Si:H thin films with respect to deposition power.

2.2.2. Resistivity

Resistivity measurements were also performed on these same films using a four point probe (see Fig. 2.1 for apparatus). These measurements yielded the total resistance in the region of the film spanned by the probes. Multiplying this resistance by a correction factor yielded the sheet resistance:

$$R_{\square} = R \cdot CF \tag{2.1}$$

which has units of Ω/□ ("ohms per square"). The correction factor, *CF*, is a dimensionless parameter which depends on the geometry of the probe relative to the film being measured.

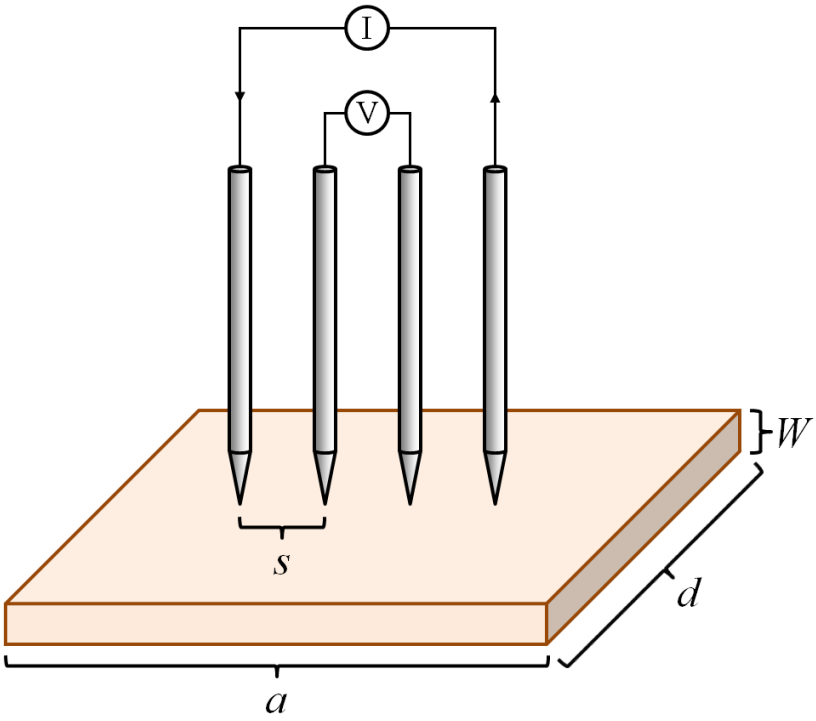

Figure 2.1: Schematic diagram of a four point probe and thin film being tested. A current is passed through the outer two probes which induces a voltage between the inner two probes. The resulting resistance can then be calculated using Ohm's law (Eq. 1.8).

In the limit where the film is much larger than the probe spacing ($d \gg s$), *CF* becomes $\pi/\ln 2$. This approximation was used for all thin films fabricated in this experiment. The sheet resistance was then multiplied by the film thickness to obtain normalized resistivities for doped a-Si:H thin films with respect to deposition power:

$$\rho = R_{\square} \cdot W \tag{2.2}$$

2.3. Results and Discussion

2.3.1. Growth Rate

Figure 2.2 shows the doped a-Si:H film growth rate as a function of the power of the PECVD process. Past literature has reported that PECVD thin film growth rates are dependent on plasma power, which in turn affects the dissociation efficiency of the feed gas [21] [32]. Higher plasma power is more efficient in decomposing the feed gases, which results in greater film growth rate [31].

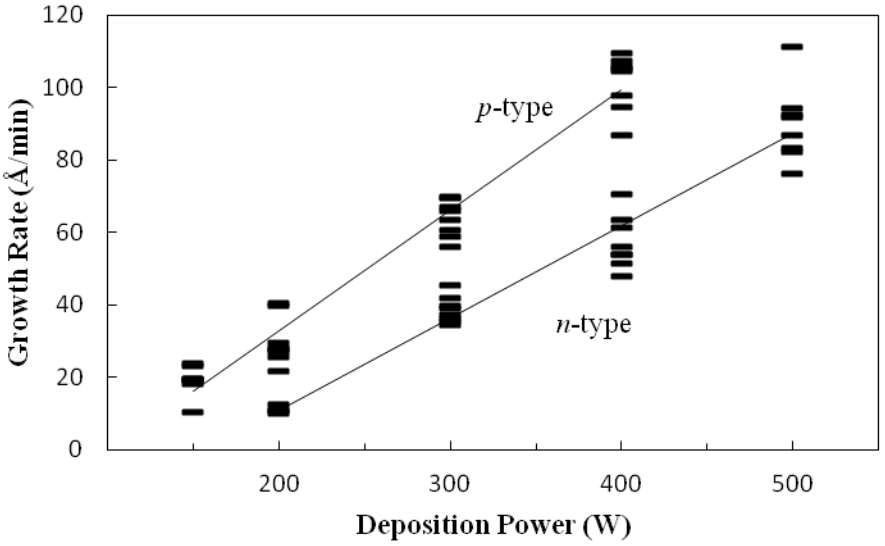

Figure 2.2: Growth rate of doped a-Si:H thin films vs. plasma power.

The Fig. 2.2 curve shows a threshold power of about 100-150 W below which the film growth is negligible and above which the deposition rate increases with increasing RF power. Since the electron energy in the plasma must be greater than the bond energies of the feed gases to dissociate them, this threshold power likely represents the minimum

power required to overcome the bond energy barrier and generate an appreciable amount of precursor radicals for film deposition.

2.3.2. Resistivity

Figure 2.3 shows the relationship between the resistivity of the doped a-Si:H thin films and deposition power. These data indicate that the resistivity of these films increases with increasing deposition power. Yan et al. experimentally verified that both the deposition rate and the charge carrier concentration (P concentration for *n*-type doping) in doped Si thin films are roughly proportional to the plasma power in an inductively-coupled plasma process, another means of plasma deposition similar to PECVD [32]. Rusop et al. reported that in doped amorphous carbon thin films deposited via PECVD, resistivity decreased with increasing deposition power [33], which would appear to contradict the results shown in Fig. 2.3.

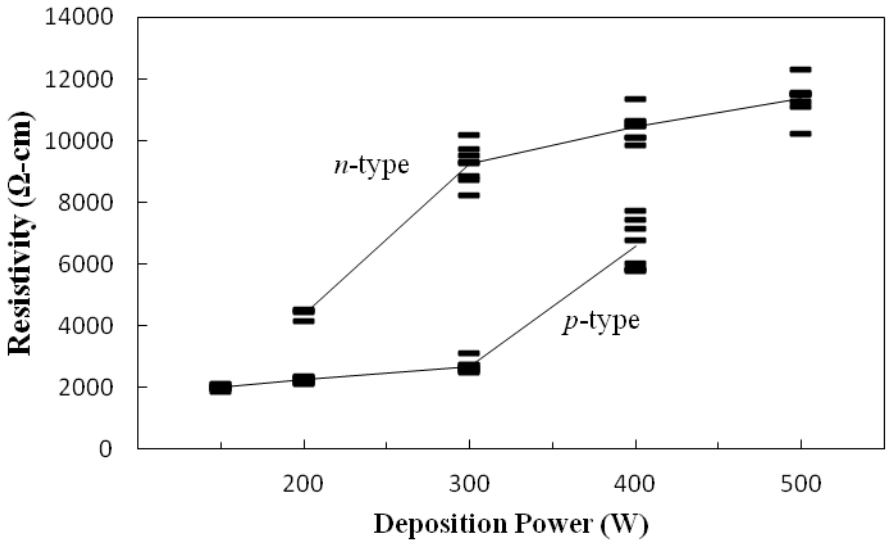

Figure 2.3: Resistivity of doped a-Si:H thin films vs. deposition power.

However, in other studies, it was shown that when the concentration of the P dopants in Si thin films was very high, resistivity would increase again [34] [35] [36]. Son et al. [34], de Nicolás et al. [37], and Sameshima et al. [38] discussed that high P concentration in Si films causes the formation of a large number of defects which serve as charge carrier recombination sites [39]. These defects reduce carrier lifespan and film conductivity [40].

Spear & Le Comber determined that the activation energy for the electrical conductivity of P-doped a-Si:H begins to increase when the P/Si ratio in the film is larger than 0.1% [9]. Since PECVD is well-suited for the deposition of thin films with very high dopant concentrations (>1%) [41], it is possible that the dopant concentrations in the films fabricated for this experiment were so high that the resistivity increased as a result. Figure 2.4 shows the conductivity of a-Si:H vs. its *n*-type doping level, with data from several sources including research done by this group. It can be seen that for the most part, conductivity increases with increasing doping level. But at extremely high doping levels (>1%), conductivity actually begins to decrease again. A more detailed analysis of the films on an atomic level would be necessary to confirm whether or not the increase in resistivity at high deposition power is indeed due to extremely high doping.

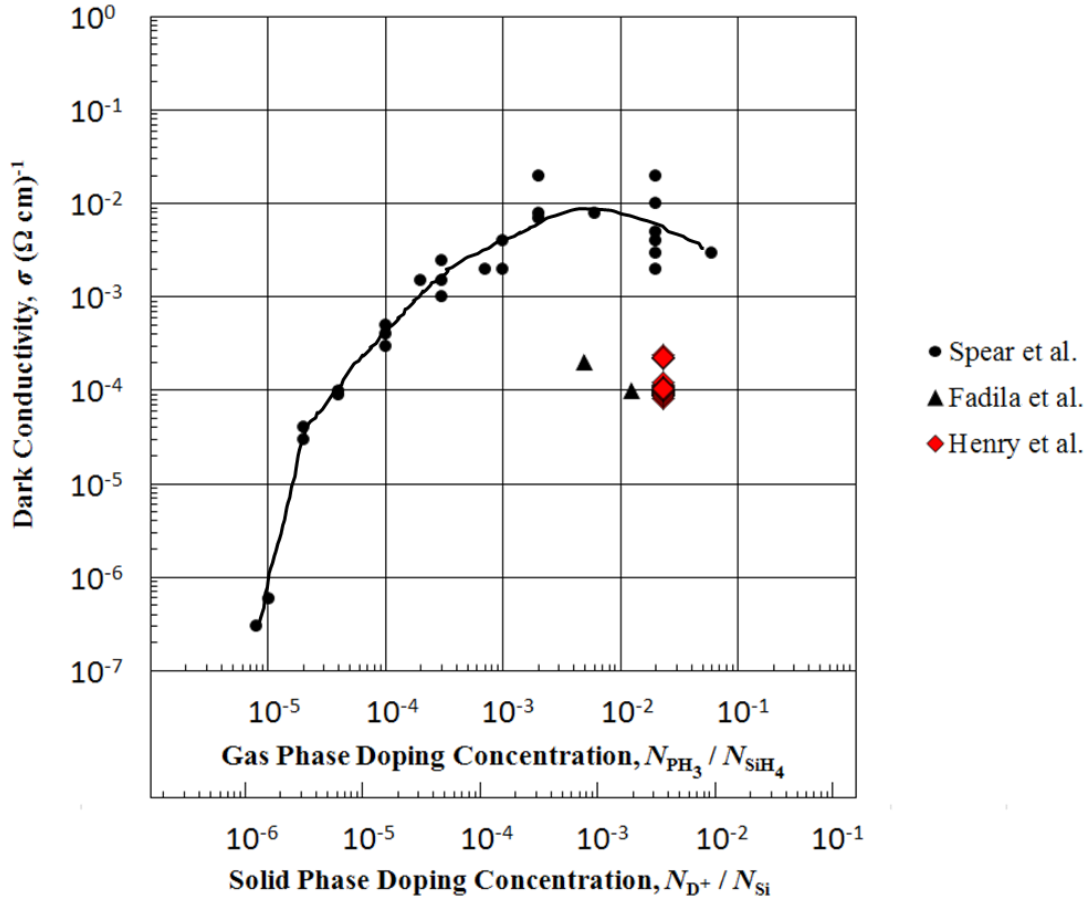

Figure 2.4: Dark conductivity of *n*-type a-Si:H vs. doping level. Note the apparent decrease in conductivity at gas phase doping levels greater than 1%. Aggregated with data from Spear & Le Comber [9] and Fadila et al. [42].

2.4. Summary

Experiment 1 has confirmed relationships between properties of n^+ a-Si:H thin films and the deposition parameters during the PECVD process. Since the remaining experiments in this thesis primarily vary the n^+ layer in PIN diodes, this experiment allows the thickness of the n^+ layer (and consequently the thickness of the whole PIN tri-layer) to be fixed for all devices to be tested, thereby eliminating a possible source of error across different fabrication conditions. While the precise values of the n^+ layer

resistivities are not used in subsequent experiments, the qualitative behavior of this relationship between resistivity and n^+ layer deposition power does provide useful insight in explaining the results of further experiments.

3. EXPERIMENT 2: EFFECT OF n^+ LAYER DEPOSITION POWER ON LIGHT SENSING OF a-Si:H PIN DIODES

This section contains portions adapted from a paper submitted in May 2016 by K. Henry and Y. Kuo [29], reproduced by permission of The Electrochemical Society.

3.1. Motivation

With the characterization of the effects of process parameters on the properties of doped a-Si:H thin films, these films could then be used in the fabrication of complete PIN diodes with the goal of determining the effects of manipulating these same process parameters on the performance and efficiency of a-Si:H thin film solar cells. Specifically, the effect of varying n^+ layer deposition power was investigated by illuminating the diode with solar light as well as red, green, and blue LED light, and recording the changes in quantum efficiency under each lighting condition.

3.2. Experimental

The fabrication of complete a-Si:H PIN diodes involves a multi-step process in addition to the deposition of the actual PIN tri-layer via PECVD. First, an 80 nm thick layer of ITO was deposited onto a Corning 1737 glass substrate using an RF magnetron sputter system. The ITO films were sputter deposited from an ITO target in Ar gas at 5 mTorr driven by RF power at 80 W and 13.56 MHz. ITO is a transparent conductive oxide, which is significantly more conductive than instrinsic a-Si:H (10^2 $(\Omega\text{-cm})^{-1}$ vs. 10^{-4} $(\Omega\text{-cm})^{-1}$). Additionally, ITO has high optical transmittance and low reflectance,

which allows most incident light to pass through this layer and reach the PIN tri-layer unimpeded [15].

After the ITO layer was deposited, all three layers of the PIN tri-layer structure were deposited using PECVD in a one pump-down process in the same chamber at a fixed temperature of 260°C. The specific conditions of each deposition layer are shown in Table 3.1 in deposition order. In order to minimize cross-contamination between consecutively deposited films the chamber was evacuated to a high vacuum (<1 mTorr) for 15 minutes between the p^+ and *i* layers and 40 minutes between the *i* and n^+ layers.

Table 3.1: Deposition conditions of a-Si:H PIN tri-layer.

	Gas Flow Rate (sccm)				Power	Pressure	Thickness
Layer	**SiH_4**	**H_2**	**B_2H_6 (2% in H_2)**	**PH_3 (7% in H_2)**	**(W)**	**(mTorr)**	**(nm)**
p^+	35	400	20	-	200	700	10
i	50	200	-	-	500	500	200
n^+	60	1000	-	20	*	700	15

*The n^+ layer was deposited at 200, 300, or 500 W for each separate diode.

Note that the p^+ and *i* layer conditions were fixed for all samples, whereas the n^+ layer deposition power was varied at 200, 300, or 500 W for each sample. Additionally, the thicknesses of all three layers including the n^+ layer were fixed. The film growth rates were determined by the method described in § 2.3.1.

After the deposition of the PIN tri-layer, another 80 nm thick layer of ITO was sputter deposited on top of the PIN stack. The top ITO layer was then patterned with a photolithography step using AZ nLOF 2020 negative photoresist. The remaining ITO was wet etched into a grid of 2 mm diameter dots using an aqua regia solution.

The complete structure of the PIN diode is shown in Figure 3.1(a). These diodes were then annealed at 200°C in air for 30 minutes to passivate defects that may have formed during the deposition or etching processes. Then, the diode characteristics were measured under light illumination with a bias voltage applied through the bottom electrode, as shown in the experimental configuration in Figure 3.1(b). Note that this illumination direction is atypical compared to the conventional direction for solar cell illumination—that is, through the p^+ layer first—as mentioned in § 1.4. Illumination through the n^+ layer was selected for this experiment since this was the layer that was being varied. Thus, changes in diode performance would be most apparent when the device was illuminated from this direction.

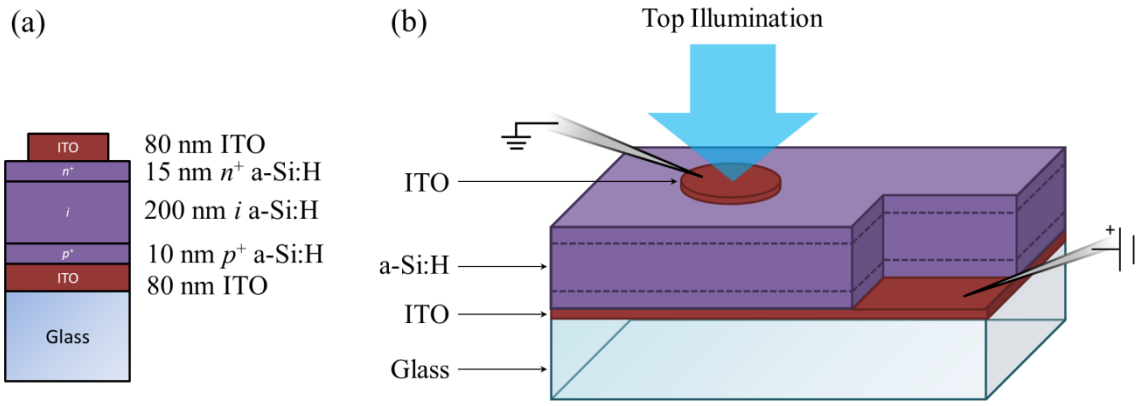

Figure 3.1: Layer structure diagram for the a-Si:H PIN diodes. This diode structure is akin to an inverted PIN superstrate structure common in solar cells [43]. The PIN diode structure with individual layer thicknesses are shown in (a). The testing configuration, indicating light illumination through the n^+ side and bias voltage applied from the bottom ITO layer, is shown in (b).

For the light sensing test, four different types of light sources were used, i.e. red (M625L3, 625 nm), green (M530L3, 530 nm), and blue (M470L3, 470 nm) Thorlabs

LEDs at a fixed power of 1.0 mW (equivalent to an intensity of 13.8 W/m^2), as well as an AM 1.5 solar simulator (Solar Light Co. Model 16S-300-002) equivalent to an intensity of 1000 W/m^2. During the light exposure, *J-V* curves were obtained with a bias voltage swept from -2 V to 1 V.

3.3. Results and Discussion

Figures 3.2, 3.3, and 3.4 show the typical *J-V* characteristics for each diode under each lighting condition. For each sample, several measurements were done on different dots to ensure that the results were consistent.

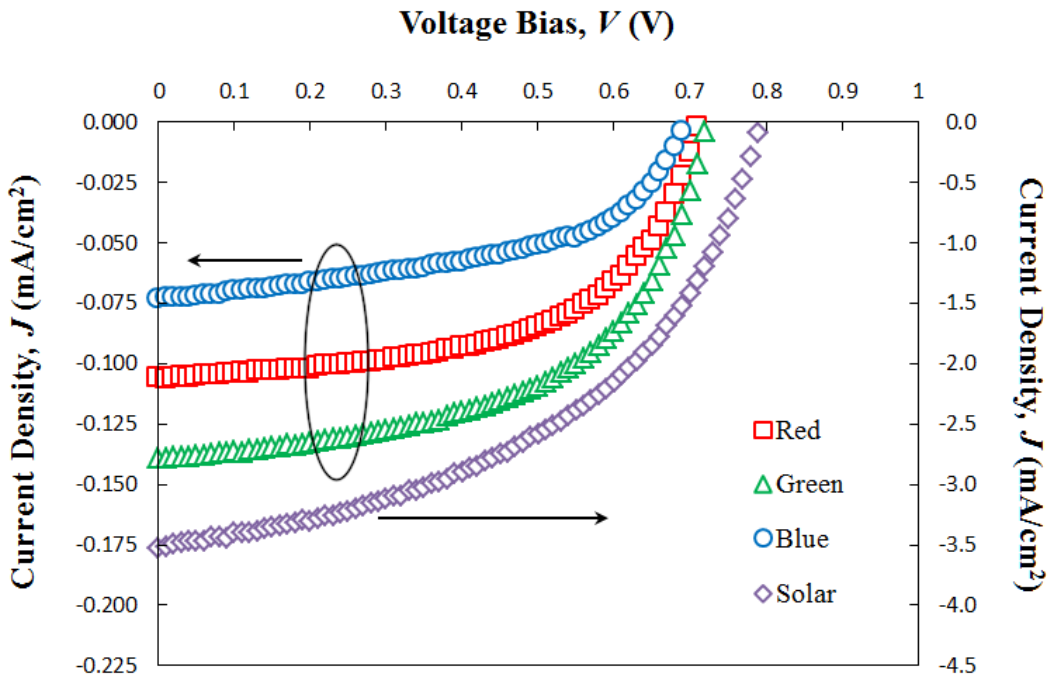

Figure 3.2: Typical *J-V* curves of the diode with n^+ layer deposited at 200 W under red, green, blue, and solar light illumination. Reproduced by permission of The Electrochemical Society.

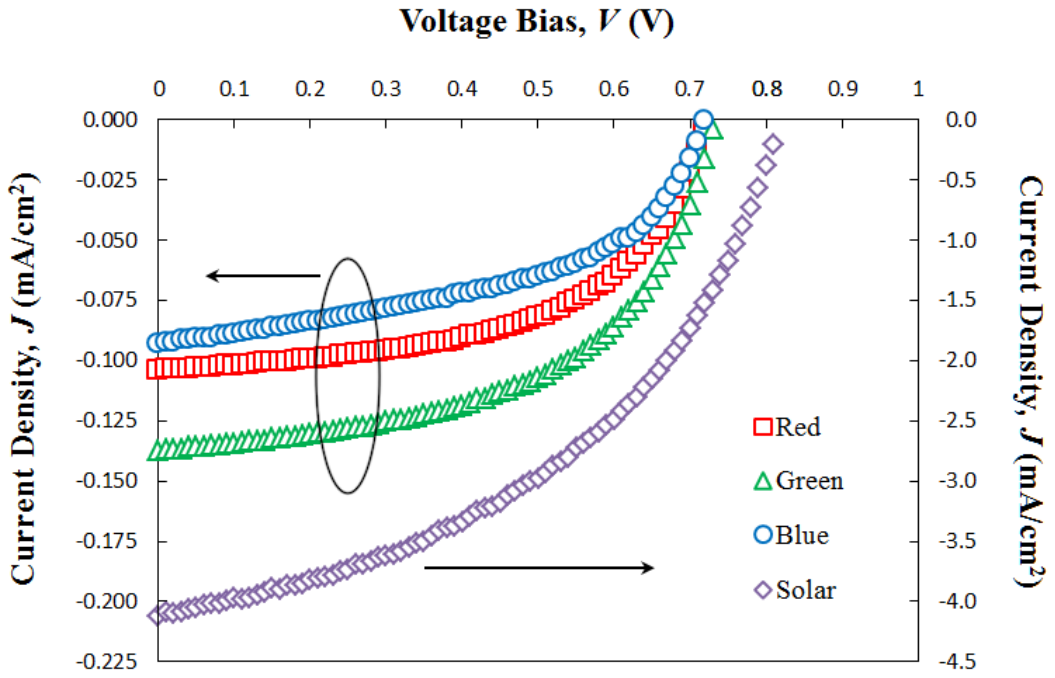

Figure 3.3: Typical *J-V* curves of the diode with n^+ layer deposited at 300 W under red, green, blue, and solar light illumination.

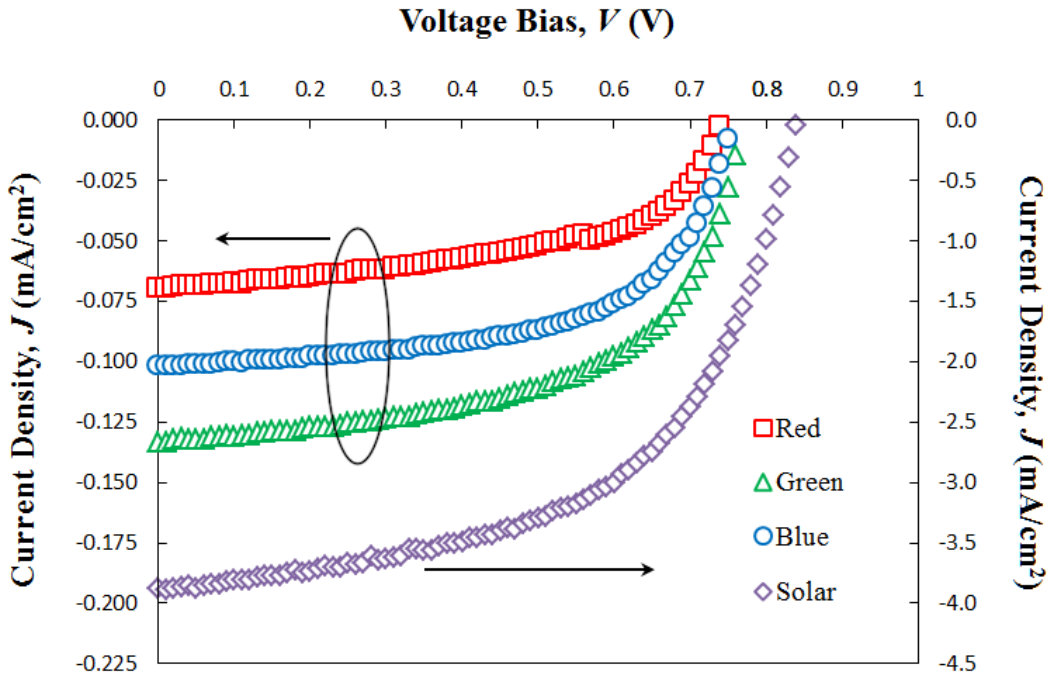

Figure 3.4: Typical *J-V* curves of the diode with n^+ layer deposited at 500 W under red, green, blue, and solar light illumination.

For all three diodes, they exhibited the greatest J_{SC} and V_{OC} under solar light illumination due its greater intensity (1000 W/m^2 vs. the LED lights' 13.8 W/m^2). On the other hand, *FF*, η, and *EQE* under solar light illumination were lower than when under the monochromatic LED illumination conditions. While visible light is composed of photons with energy equal to or slightly above the E_g of a-Si:H (1.9-2.5 eV vs. 1.8 eV), solar light contains a significant fraction of photons that are either less energetic or far more energetic than the band gap of a-Si:H [44] [45]. This means that a large portion of incident solar light is not used to generate excitons and is simply wasted as thermal energy [46]. See Appendix A for a plot of the spectral irradiance for AM 1.5 solar light. Tables 3.2, 3.3, and 3.4 list the optical characteristics determined from the Fig. 3.2, 3.3, and 3.4 curves.

Table 3.2: Optical characteristics of the diode with n^+ layer fabricated at 200 W.

Color	V_{OC} **(V)**	J_{SC} **(mA/cm^2)**	***FF***	η **(%)**	***EQE* (%)**	R_S **(kΩ)**	R_{SH} **(kΩ)**
Red	0.711	-0.0986	0.57	2.89	14.17	27.9	2404
Green	0.723	-0.1285	0.54	3.66	21.77	24.3	1336
Blue	0.694	-0.0637	0.52	1.67	12.17	46.5	1378
Solar	0.793	-3.237	0.47	1.21	4.57	1.60	39.7

Table 3.3: Optical characteristics of the diode with n^+ layer fabricated at 300 W.

Color	V_{OC} **(V)**	J_{SC} **(mA/cm^2)**	***FF***	η **(%)**	***EQE* (%)**	R_S **(kΩ)**	R_{SH} **(kΩ)**
Red	0.721	-0.0969	0.55	2.52	12.67	32.8	2180
Green	0.739	-0.1391	0.53	3.97	23.58	24.8	1302
Blue	0.724	-0.0929	0.49	2.39	17.75	37.8	949
Solar	0.820	-4.241	0.44	1.54	5.99	1.51	28.2

Table 3.4: Optical characteristics of the diode with n^+ layer fabricated at 500 W.

Color	V_{OC} **(V)**	J_{SC} **(mA/cm^2)**	***FF***	η **(%)**	***EQE* (%)**	R_S **(kΩ)**	R_{SH} **(kΩ)**
Red	0.748	-0.0652	0.55	1.94	9.37	38.6	1971
Green	0.774	-0.1343	0.57	4.32	22.76	19.2	1568
Blue	0.761	-0.1026	0.59	3.34	19.61	23.5	2170
Solar	0.847	-3.796	0.55	1.77	5.36	1.15	51.4

Under monochromatic LED illumination, the influence of the n^+ layer deposition power on diode light sensitivity was apparent. For each individual diode, the largest J_{SC} was observed under green light illumination. On the other hand, V_{OC} was only slightly influenced by the wavelength of incident light. This can be explained by the following relationship between J_{SC} and V_{OC}:

$$J_{SC} = J_S \exp\left(\frac{qV_{OC}}{AkT}\right) \tag{3.1}$$

where A is the diode quality factor [47], J_S is the diode saturation current density, which is roughly the maximum absolute value of J reached under very large negative bias voltages just before the breakdown voltage (see Fig. 1.6(b)). Eq. 3.1 can also be rearranged as:

$$V_{OC} = \frac{AkT}{q} \ln\left(\frac{J_{SC}}{J_S}\right) \tag{3.2}$$

From Eqs. 3.1 and 3.2, it is clear that V_{OC} is proportional to the natural logarithm of J_{SC}. Therefore, little change in V_{OC} can be expected for changes in J_{SC}.

The behavior of each diode under red and blue light is more complex. Under red light illumination, the magnitude of J_{SC} decreased with an increase in n^+ deposition power. Under blue light illumination, the opposite effect was observed. This behavior was most apparent in the *J-V* curves when the n^+ layer deposition power was changed from 300 to 500 W (Figs. 3.3 and 3.4), where it can be seen that the order of increasing $|J_{SC}|$ changes from blue→red→green to red→blue→green.

When *EQE* is used as the parameter for diode performance, as shown in Figure 3.5, it can also be seen that the behavior of these diodes under red and blue light

exhibits divergent trends. To explain this, one must examine the ability for a-Si:H to absorb incoming light with respect to light wavelength. Most commonly, this is represented as the absorption coefficient, α, which is essentially the effectiveness with which a material can absorb incoming photons as a function of photon energy.

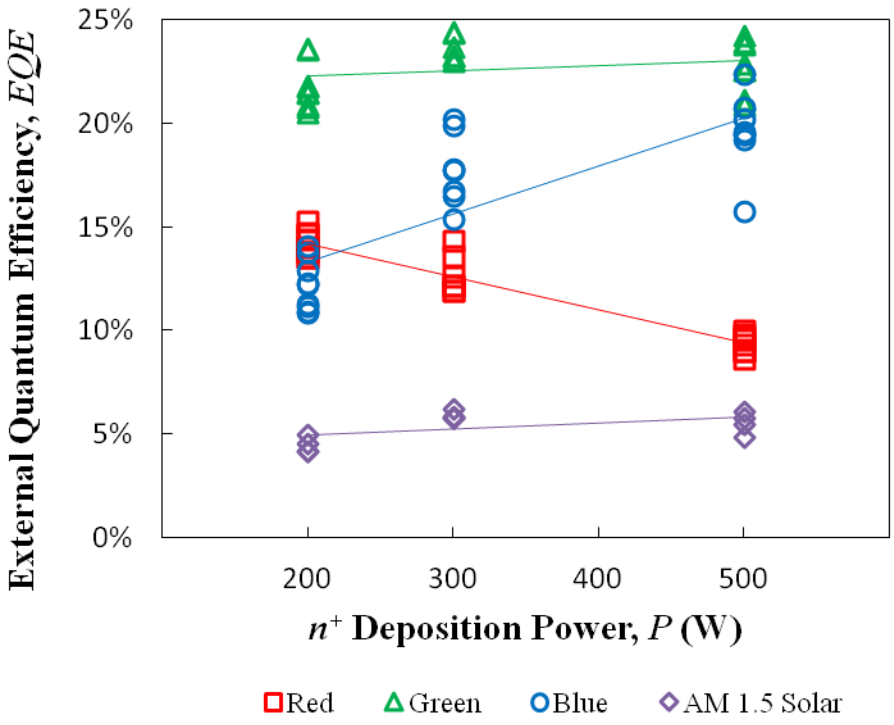

Figure 3.5: *EQE* vs. n^+ deposition power under red, green, blue, and solar light illumination. Reproduced by permission of The Electrochemical Society. See Appendix B for plots of remaining optical properties under red, green, and blue light.

A plot of α vs. photon energy for various phases of Si is shown in Figure 3.6. It can be seen that for all types of Si, α increases with increasing photon energy. In general, the higher the value of α, the better the photon absorption efficiency is. This explains why the *EQE* of the PIN diodes are higher under green light illumination than under red light. However, this does not explain why *EQE* is low under blue light illumination.

The ability for light to penetrate through a-Si:H is dependent on the wavelength of the incoming light, which is directly related to α. Long wavelength, low energy light, e.g. >570 nm, is not effectively absorbed by a-Si:H. Therefore, it mostly transmits through films as thick as 280 nm [48].

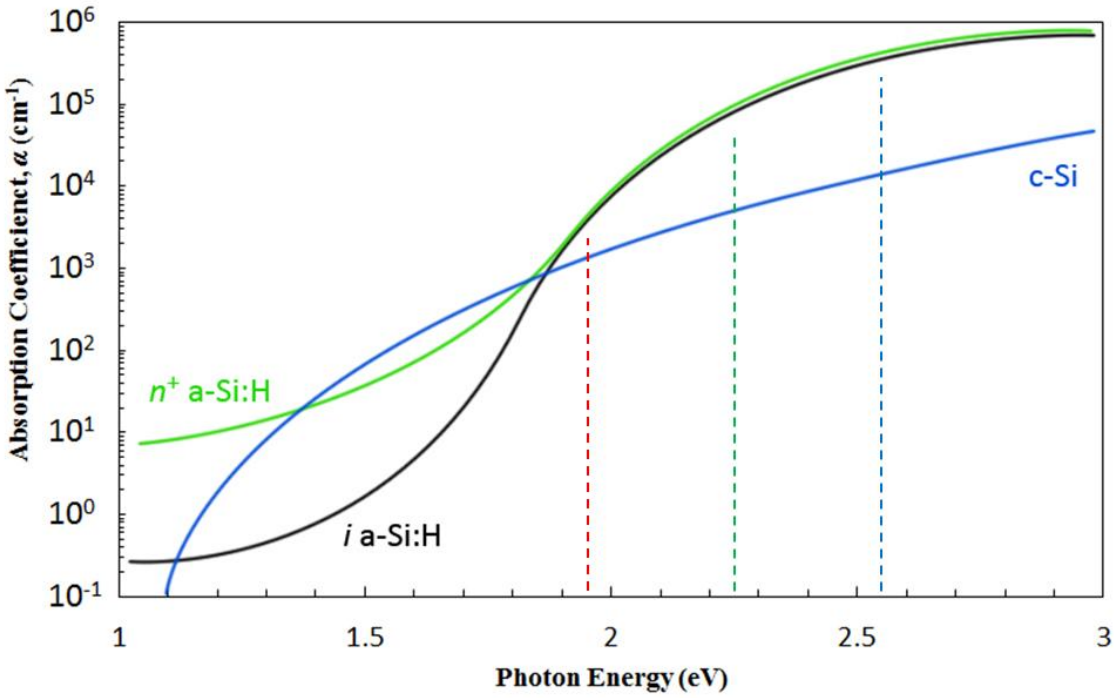

Figure 3.6: Absorption coefficient of Si vs. incident photon energy. The amount of energy imparted by photons of red, green, and blue light is indicated by the leftmost, middle, and rightmost dashed lines, respectively. Aggregated with data from Shah [20], Tiedje et al. [49], and Jovanov et al. [50].

On the other hand, shorter wavelength light, e.g. <500 nm, is almost completely absorbed by a-Si:H films as thin as 100 nm [51]. Figure 3.7 shows the dependence of light penetration depth on photon energy for the PIN diodes in this work.

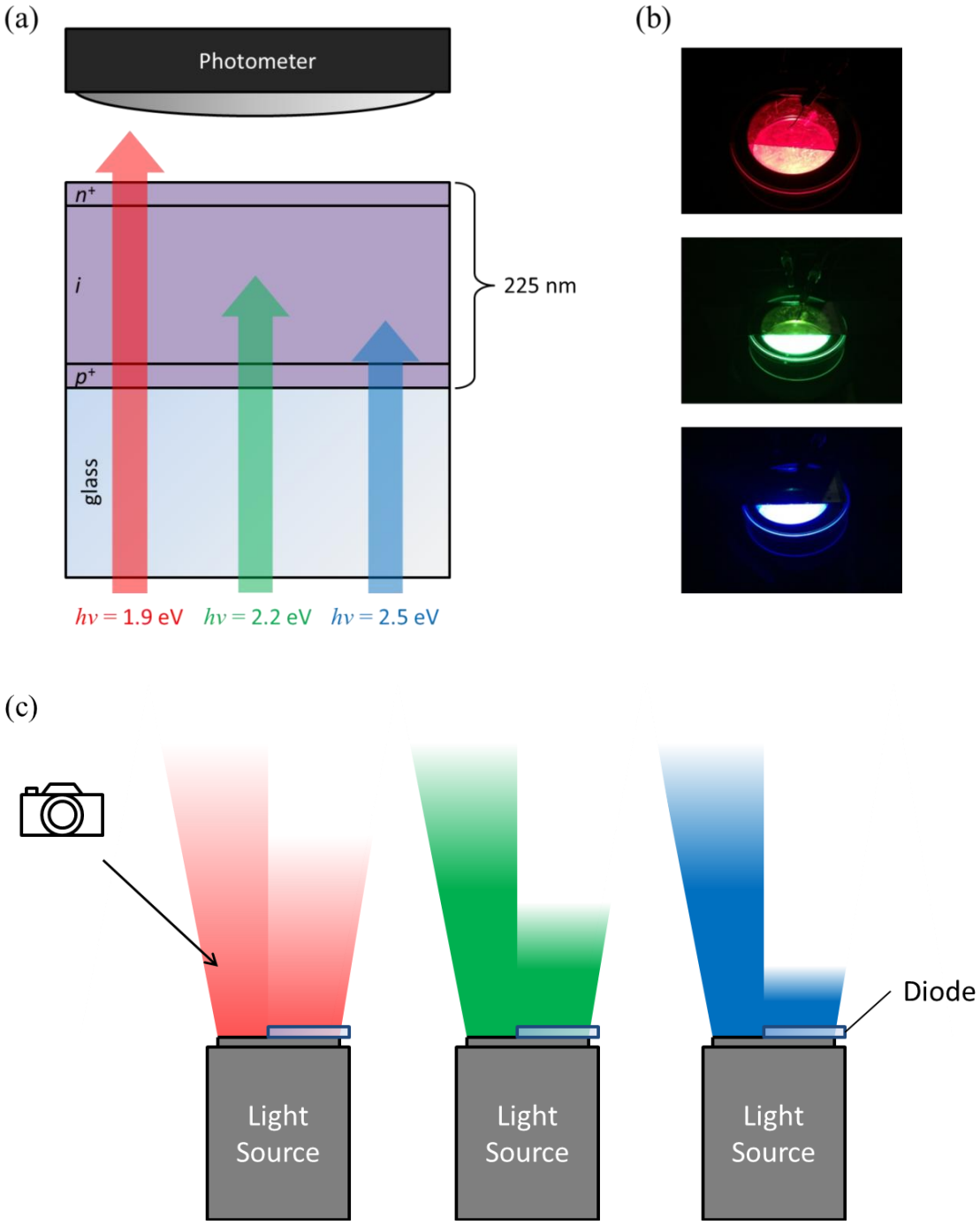

Figure 3.7: (a) Relative light penetration depth into an a-Si:H PIN diode with respect to photon energy. (b) Photos of light transmittance with respect to incident photon energy for the PIN diodes prepared in this work. (c) Device arrangement used to capture the photos in (b), wherein the partially covered light source served to illustrate the relative degree to which a-Si:H absorbed each color of incoming light.

It can be seen that low energy light is able to transmit through the tri-layer without being totally absorbed. High energy blue light is almost fully absorbed by the same diode. Since photons from blue light illumination are so effectively absorbed, it is natural to expect that blue light illumination would yield a the highest value of J_{SC} for all deposition conditions. But because of its large α value, most of the blue light is absorbed in the n^+ layer or at the *i/n* interface. Therefore, the *EQE* of these PIN diodes under blue light illumination is lower than for other illumination conditions.

The question remains, however, of why the trend of *EQE* with respect to n^+ layer deposition power differs between red light and blue light illumination conditions. Under blue light illumination, *EQE* increased with respect to n^+ layer deposition power, but under red light, *EQE* decreased with increasing deposition power. As mentioned in § 2.3.2, increasing doping concentration in *n*-type a-Si:H increases the defect density [39]. Therefore, the number of defects present between E_C and E_V increases with increasing n^+ deposition power, reducing *EQE* under red light. Since excitons generated by blue light absorb enough photon energy to bypass the band gap, they were less affected by the presence of defect states. This effect also explains why in Fig. 3.6, α increases in the low photon energy regime from undoped to doped a-Si:H. Figure 3.8 shows the results of transmittance testing of these PIN a-Si:H diodes, which also implies an increase in α for low energy photons. It can be seen that as the n^+ layer deposition power increased, the transmittance of red light through the diodes decreased due to the defect-induced parasitic light absorption [20]. Because only the n^+ layer deposition conditions were changed for each sample, it is reasonable to conclude that the

discrepancy in absorbed light occurs in the n^+ layer or at the *i/n* interface. On the other hand, the transmittance of green and blue light was extremely low (on the order of 1% and 0.01%, respectively), and was much less affected by n^+ deposition power. This suggests that the primary mechanism at play in this experiment was the formation of defect states in the midgap of *n*-type a-Si:H as a result of varying RF power supplied during the deposition these a-Si:H thin film diodes, but further physical analysis is necessary to confirm this.

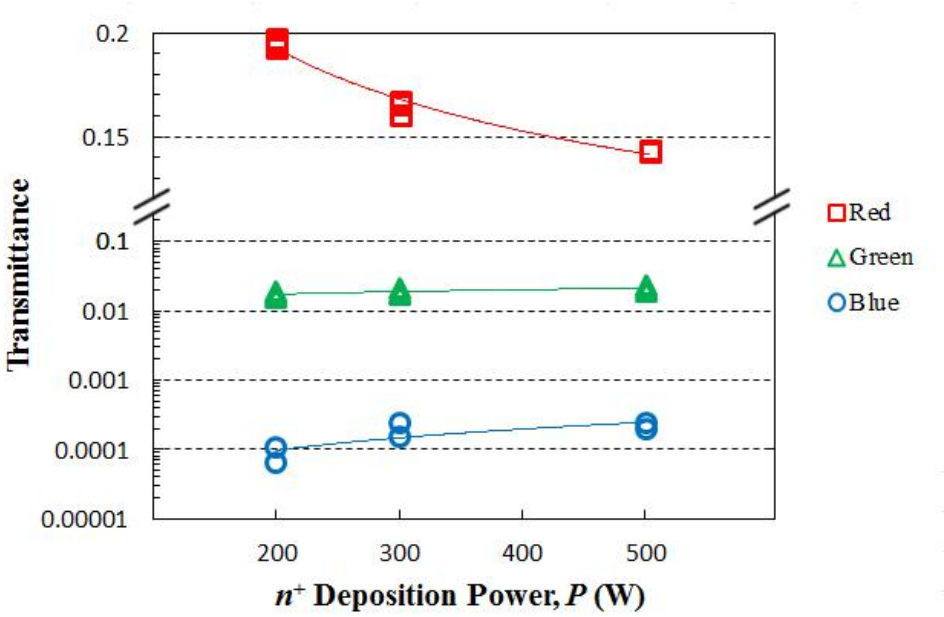

Figure 3.8: Optical transmittance through the a-Si:H PIN diode vs. n^+ layer deposition power. Reproduced by permission of The Electrochemical Society.

3.4. Summary

Three different conditions were employed during the fabrication of a-Si:H thin films diodes. The only process parameter that was varied across the diodes was the amount of RF power supplied during the deposition of the n^+ layer in the PECVD step of

the overall fabrication process. The diodes were illuminated with different color lights and their *J-V* curves were generated under voltage bias. Device characteristics such as V_{OC}, J_{SC}, *FF*, η, *EQE*, R_S, and R_{SH} were calculated from these curves. *EQE* was used as the parameter to determine the performance of each diode.

The n^+ layer deposition power has significant influence on the light sensitivity of a-Si:H PIN diodes. In this experiment's testing configuration, incident light passed through the n^+ layer before reaching the underlying *i* and p^+ layers. The absorption of light was dependent on the wavelength of the incident light. Varying the RF power during the deposition of the n^+ layer affected the concentration of dopants in the film as well as the density of defects, both of which affected the diode's light sensing ability. The ability for an a-Si:H PIN diode to function is dependent on the ability of incoming photons to generate excitons in the *i* layer, which in turn is affected by properties of the n^+ layer that the photons pass through as well as the photon energy.

4. EXPERIMENT 3: EFFECT OF INCIDENT LIGHT DIRECTION AND REFLECTOR CONFIGURATION ON LIGHT SENSING OF a-Si:H PIN DIODES

4.2. Motivation

With the effect of n^+ layer deposition power on diode light sensitivity understood, other parameters that were important to the performance of a-Si:H PIN thin film diodes were studied. Most PIN solar cells and photodiodes are oriented such that incident light enters through the p^+ layer. This is because in general, excitons are generated nearer to the side that the incoming light enters from. By illuminating through the *p*-side, holes do not need to travel as far through the diode as electrons do [52]. This is advantageous because holes have lower mobility [15], so minimizing their travel distance improves diode performance. Additionally, most solar cell structures include a back reflector on the far side of the PIN structure. This allows light that is not absorbed effectively by the diode—especially low energy photons—to be scattered and reflected back into the *i* layer to further increase excitons generation.

The aim of this experiment was to determine the difference in the quantum efficiency of a-Si:H PIN diodes when illuminated through the n^+ layer vs. when illuminated through the p^+ layer. Additionally, diodes were fabricated with metallic reflectors added to either the top or bottom ITO electrodes to examine the effect of these reflectors on light detection.

4.3. Experimental

A-Si:H PIN thin film diodes were fabricated using the method described in experiment 2 (§ 3). The n^+ layer deposition power in these samples was fixed at 500 W because the difference in *EQE* between red light and blue light illumination was the largest for the diode fabricated with this condition. An aluminum reflector layer was sputter deposited either before the deposition of the bottommost ITO layer or after the topmost ITO layer, for a total of three different diode structures. Figure 4.1 shows the layer structure of each diode, one with a top reflector (Fig. 4.1(a)), bottom reflector (Fig. 4.1(b)), or no reflector (Fig. 4.1(c), which are named TR, BR, and NR, respectively. The For all three samples, the PIN tri-layers were deposited at the same time to minimize any PECVD process variations. For each diode, three types of LED incident lights, i.e. red (625 nm), green (530 nm), and blue (470 nm) with a fixed intensity of 13.8 W/m^2, were used as the illumination sources. J-V curves were generated under applied bias voltage for each diode and all possible illumination conditions.

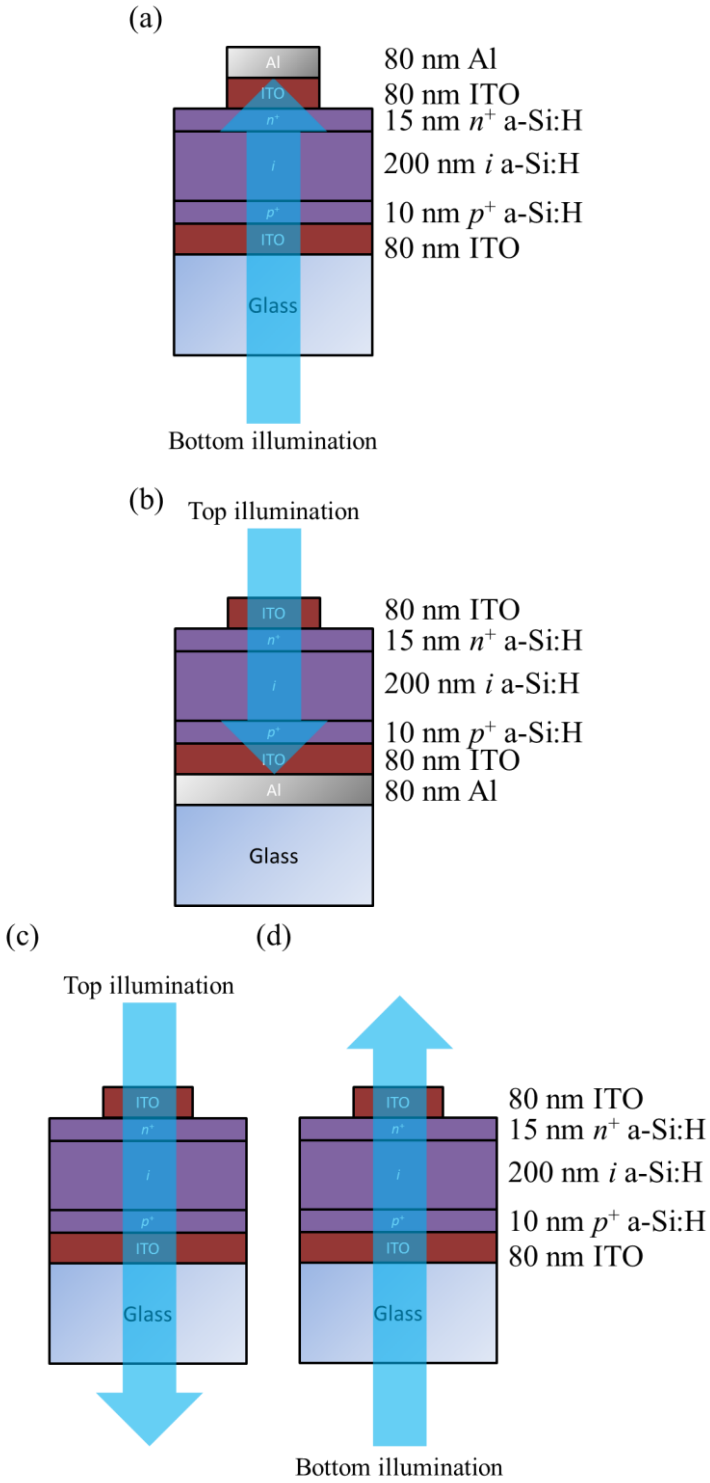

Figure 4.1: Layer structures for the (a) TR diode with incident light through the n^+ layer, the (b) BR diode with incident light through the p^+ layer, and the NR diode with incident light through the (c) n^+ or (d) p^+ layer.

4.4. Results and Discussion

Based on each diode's allowed illumination direction, four sets of *J-V* curves were measured, as shown in Figure 4.2. From a cursory graphical analysis, it can be seen that regardless of illumination direction, all diodes exhibited improved performance, e.g. higher *EQE*, with a metallic reflector (Figs. 4.2(c) and (d)) than without (Figs. 4.2(a) and (b)). This effect is most obvious in the red light illumination condition because, as mentioned in § 3.3, red light is less absorbed by a-Si:H compared to green or blue light. Without a reflector layer, incoming red light passes through the PIN tri-layer without being fully absorbed. When a back reflector is included, unabsorbed red light is reflected back into the tri-layer for further exciton generation. Since blue light is almost completely absorbed before reaching the *i* layer, the *J-V* curves are not significantly affected by the existence of a reflector layer under the blue light illumination condition. Additionally, these curves appear to be of higher quality when illuminated from the bottom (Figs. 4.2(b) and (d)) than when illuminated from the top (Figs. 4.2(a) and (d))—especially under blue light—based on their greater area enclosed and by the flatter slope through the y-axis, e.g. higher absolute values of R_{SH} and J_{SC}. This is due to two factors mentioned earlier: blue light is almost completely absorbed even by thin layers of a-Si:H, which minimizes wasted photons; and incident light that enters through the *p*-side creates excitons closer to the p^+ layer. The latter factor of which is ideal because electrons, with higher lifetimes than holes, will travel further through the diode than holes [52].

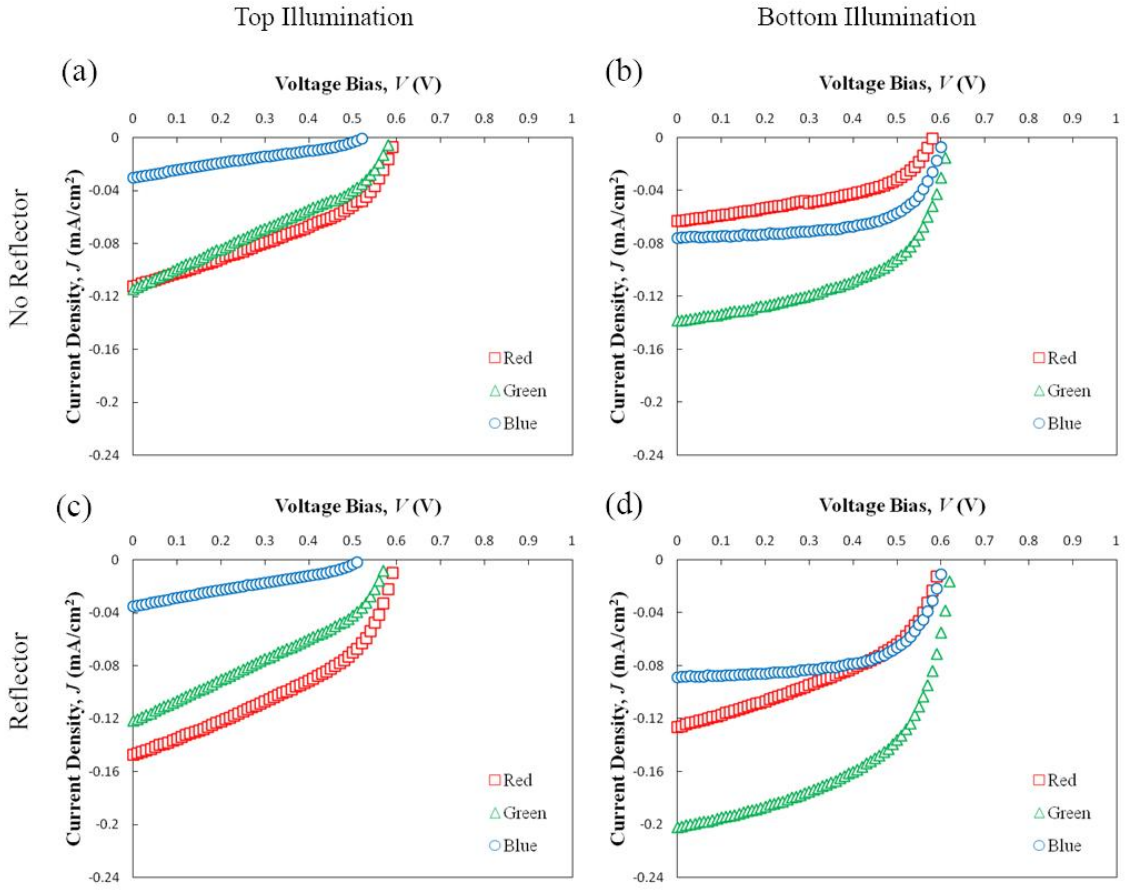

Figure 4.2: Typical *J-V* characteristics under red, green, and blue light for each diode and all possible illumination directions. The NR diode was illuminated from the top (a) and from the bottom (b), while the BR diode was only illuminated from the top (c) and the TR diode was only illuminated from the bottom (d).

Figure 4.3 shows *EQE* vs. incident light wavelength under top (Fig. 4.3(a)) and bottom (Fig. 4.3(b)) illumination conditions calculated from the Fig. 4.2 curves. These plots also indicate that the inclusion of a back reflector always improved the efficiency of the diode. From these curves, the remaining optical properties were calculated and are listed in Tables 4.1, 4.2, 4.3, and 4.4.

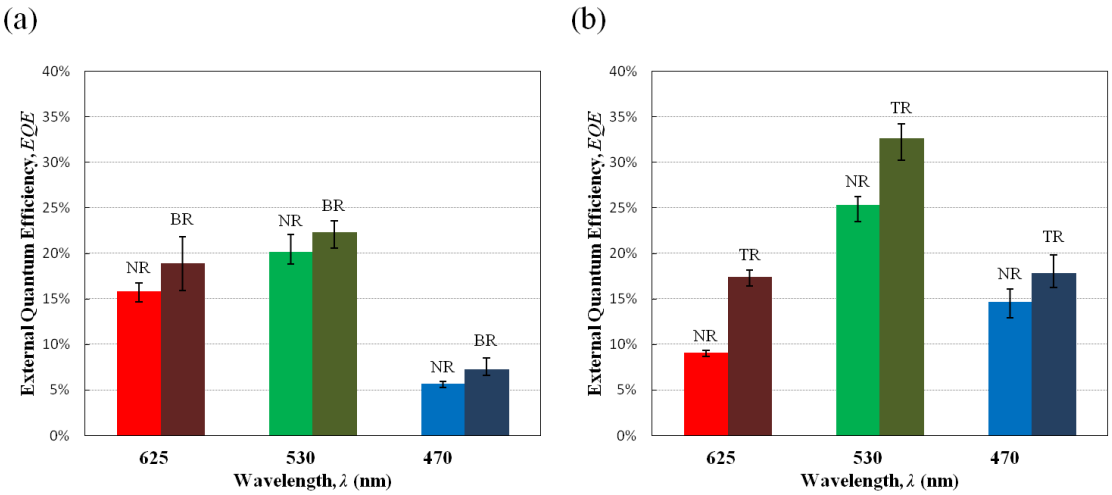

Figure 4.3: *EQE* vs. incident light wavelength of diodes with and without back reflectors, when under (a) top illumination and (b) bottom illumination. Error bars indicate full range of data for each condition. See Appendix C for plots of remaining optical properties.

An unusual result that can be seen from Fig. 4.2 is that, although the diodes exhibited better *EQE* under green and blue light when illuminated from the bottom, the *EQE* of the NR diode was actually worse under red light when illuminated from the bottom. When a reflector was included, i.e. the BR and TR diodes, the difference in *EQE* between the two under red light illumination was within the margin of error.

Table 4.1: Optical characteristics of the NR diode under top illumination.

Color	V_{OC} **(V)**	J_{SC} **(mA/cm^2)**	***FF***	η **(%)**	***EQE* (%)**	R_S **(kΩ)**	R_{SH} **(kΩ)**
Red	0.60	-0.1105	0.41	1.96	15.87	27.6	351
Green	0.59	-0.1151	0.33	1.61	20.14	33.5	214
Blue	0.53	-0.0299	0.27	0.31	5.71	137	538

Table 4.2: Optical characteristics of the NR diode under bottom illumination.

Color	V_{OC} **(V)**	J_{SC} **(mA/cm^2)**	***FF***	η **(%)**	***EQE* (%)**	R_S **(kΩ)**	R_{SH} **(kΩ)**
Red	0.59	-0.0633	0.46	1.25	9.09	37.9	779
Green	0.63	-0.1496	0.54	3.64	25.35	15.81	745
Blue	0.61	-0.0766	0.63	2.13	14.64	27.2	4460

Table 4.3: Optical characteristics of the BR diode under top illumination.

Color	V_{OC} (V)	J_{SC} (mA/cm^2)	*FF*	η (%)	*EQE* (%)	R_S (kΩ)	R_{SH} (kΩ)
Red	0.60	-0.1318	0.42	2.40	18.94	23.0	328
Green	0.58	-0.1319	0.34	1.89	22.34	30.1	201
Blue	0.53	-0.0383	0.28	0.41	7.31	117	446

Table 4.4: Optical characteristics of the TR diode under bottom illumination.

Color	V_{OC} (V)	J_{SC} (mA/cm^2)	*FF*	η (%)	*EQE* (%)	R_S (kΩ)	R_{SH} (kΩ)
Red	0.61	-0.1215	0.43	2.32	17.46	21.5	389
Green	0.63	-0.1927	0.54	4.73	32.66	11.87	588
Blue	0.62	-0.0933	0.62	2.59	17.84	23.8	3796

In 1995, Wieczorek. measured the response characteristics (transient photocurrent behavior) of a-Si:H PIN photodiodes when reverse biased and illuminated from either direction by monochromatic red, green, and blue light. They noted that the effect of illumination direction on photocurrent behavior was closely related to the carrier mobility and lifetime within the illuminated depth of the photodiode [53]. It is well known that the lifetime of holes is much lower than the lifetime of electrons in a-Si:H diodes [19]. Electrons and holes generated within the *i* layer of PIN diodes must travel to the n^+ layer or p^+ layer, respectively, in order to generate a current. Figures 4.4, 4.5, and 4.6 show conceptual diagrams of the light absorption profiles, as well as the electron and hole distributions, as a function of depth under red, green, and blue light, respectively. Absorption profiles are based on the relative absorption coefficients of a-Si:H for various photon energies, and the carrier distributions are based on insights from Wieczorek. [53]. This paper developed a model for carrier distribution under green light illumination, and additional figures were generated for red and blue light based on the known differences in absorptivity for these light colors. Because green and blue light is

more effectively absorbed, the majority of excitons are generated near the window layer. When this window layer is the p^+ layer, photogenerated holes travel less distance to reach the p^+ layer than the photogenerated electrons travel to reach the n^+ layer. This is why the diodes experience higher *EQE*s under green and blue light when illuminated from the *p*-side. Under the red light illumination condition, holes are generated more uniformly throughout the *i* layer. Therefore, the average hole travel distance does not change much with respect to illumination direction under red light.

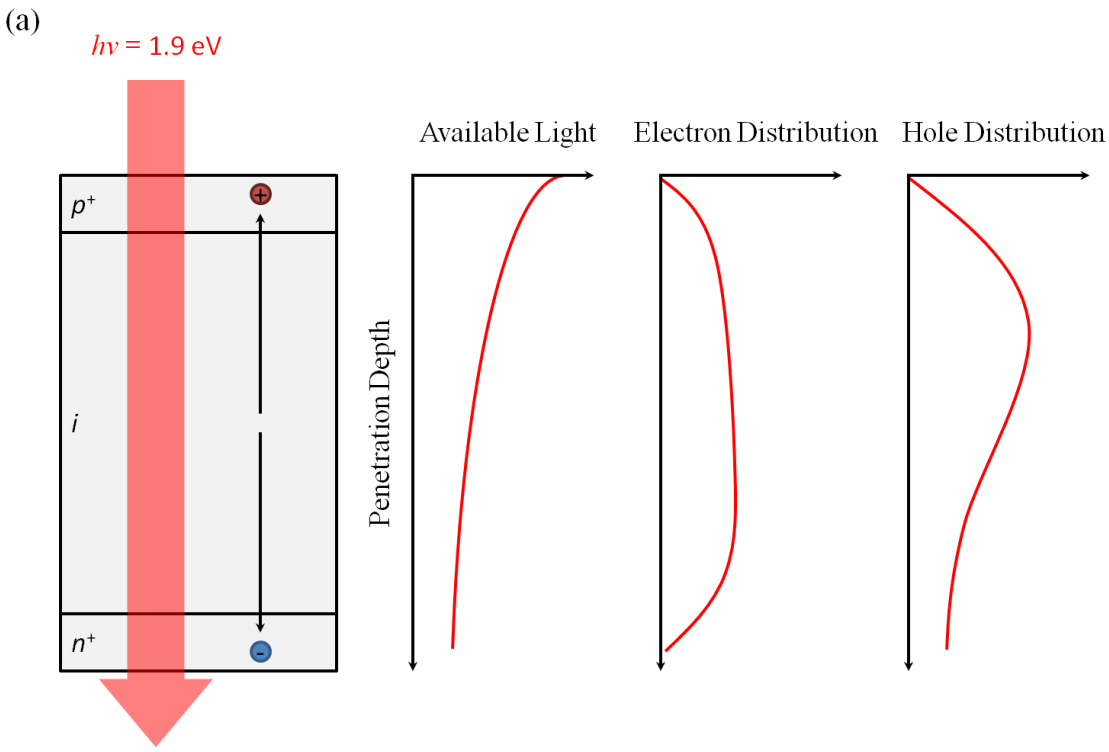

Figure 4.4: Light penetration profiles and exciton distribution profiles for bottom illumination and net reverse bias under red light.

(b)

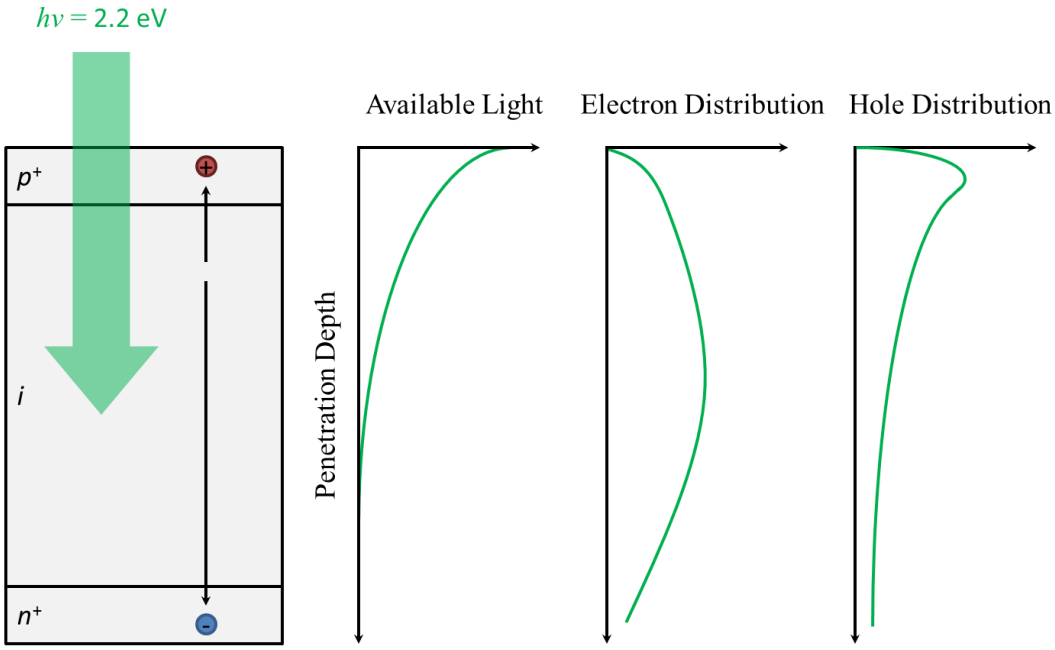

Figure 4.5: Light penetration profiles and exciton distribution profiles for bottom illumination and net reverse bias under green light.

(c)

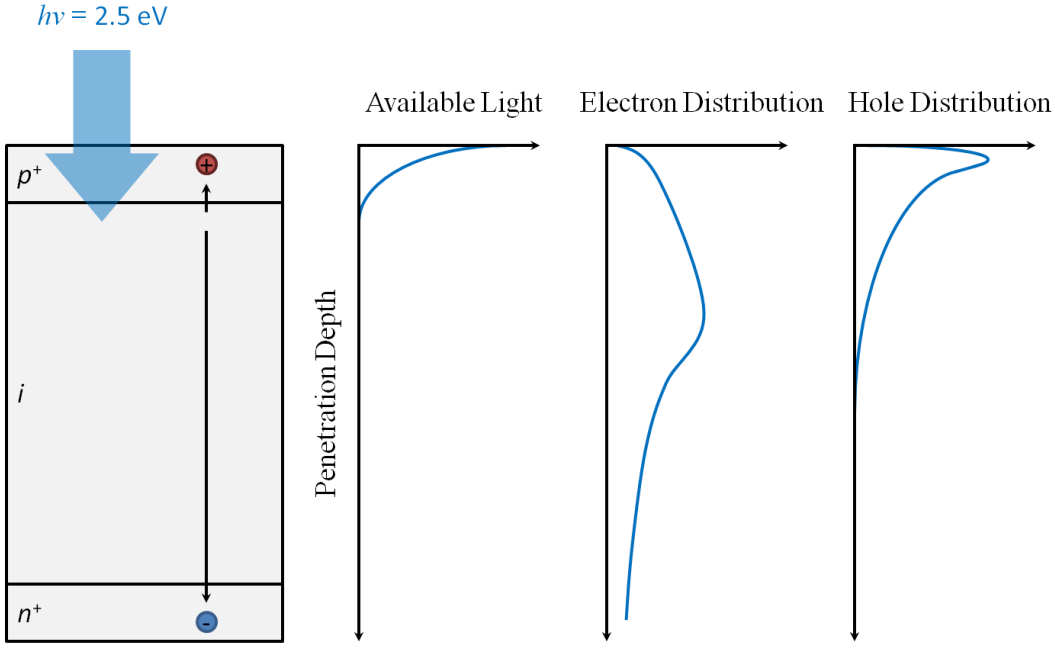

Figure 4.6: Light penetration profiles and exciton distribution profiles for bottom illumination and net reverse bias under blue light.

The effect of defect states on charge carrier recombination as mentioned in § 3.3 may present a possible explanation for the lower *EQE* that the diodes exhibited when illuminated by red light from the bottom. In experiment 2, it was determined that in the diodes fabricated with the highest n^+ layer deposition power, red light illumination exhibited the lowest *EQE*. This same deposition power was again used for experiment 3's diodes. Here, when red light is shined through the n^+ layer, more electrons are generated nearer to the window layer for charge carrier exit. But when red light is shined through the p^+ layer, electrons must travel further on average to complete the circuit, meaning they are more likely to encounter recombination events before drifting near the *i/n* interface. Normally, it is beneficial for electrons to travel further than holes through a-Si:H because of electrons' greater lifetime. But, if the defect density near the *i/n* interface is very high, as was postulated in § 2.3.2 [34] [37] [38], then the likelihood of electron recombination may increase. If electron recombination indeed becomes more limiting than hole lifetime due to the high defect density of the *i/n* interface, this could potentially explain the lowered *EQE* of the diodes when illuminated by red light through the p^+ layer, though more experimentation and/or analysis would be needed to verify this claim.

4.5. Summary

Three different types of a-Si:H PIN diodes were fabricated under the same PECVD condition. The main difference among these diodes was the inclusion of an Al reflecting layer: either above the topmost ITO layer, below the bottommost ITO layer, or not included at all. *J-V* curves under different illumination conditions and directions

were measured. Parameters such as V_{OC}, J_{SC}, *FF*, η, *EQE*, R_S, and R_{SH} were all derived from these plots, and *EQE* was used as the primary parameter to compare the diode performance.

The direction of incident light significantly affected the performance of the diode. Conventional solar cells are primarily illuminated through the p^+ layer, and these diodes exhibited better EQE when illuminated through the p^+ layer for most wavelengths of incident light. The diodes showed a slight decrease in *EQE* under red light when illuminated from the p^+ layer, and this was believed to be due to the limiting factors of charge carrier mobility. Red light generates charge carriers more uniformly throughout the *i* layer. Because electrons photogenerated by red light illumination had to travel further than under other light colors, they were more likely to encounter recombination events near the *i/n* interface, which potentially reduced the overall current and consequently the *EQE*. When illuminated through the *n*-side, by blue and green light illumination yielded lower *EQEs* compared to the same illumination condition through the *p*-side because holes, which have lower carrier lifetimes than electrons, had to travel further through the *i* layer. Under blue and green light illumination through the *n*-side, electrons were generated nearer to the n^+ layer so their lifetimes were not a limiting factor. The inclusion of a metallic reflector layer consistently improved the *EQE* of each diode. This effect was most pronounced for red light illumination because of a-Si:H's poorer absorption of low energy photons. For the green and blue light illumination conditions, the inclusion of a metallic reflector layer only slightly improved the *EQEs*

because most of the higher energy photons were absorbed in the p^+ or n^+ layer, during illumination from the *p*- or *n*-side, respectively.

5. CONCLUSIONS

The use of semiconductor materials in photovoltaic device is a rapidly expanding field. Thin film solar cells are one of many potential types of photodiode devices. These devices employ a PIN doping configuration which allows for the separation of oppositely charged excitons and the conduction of a current as a result. a-Si:H is a common material for the fabrication of thin film solar cells and photodiodes due to its relatively low material costs and high durability compared to other types of photovoltaics. A-Si:H PIN thin film diodes can be fabricated in a simple process known as PECVD. This method presents the additional advantage of allowing for the *in situ* doping of the diode which further simplifies the fabrication process of the diodes. Using PECVD to deposit the tri-layer structure of the diode, three experiments were conducted to explore the effect of varying several process parameters on the light sensing ability of PIN diodes.

The first experiment verified the effect of varying RF power on the deposition of doped a-Si:H thin films during the PECVD process. The resulting effect on film growth rate and resistivity were measured. Film growth rate varied roughly linearly with RF power, and resistivity increased nonlinearly with increasing RF power.

Using the results from experiment 1, the second experiment—wherein complete PIN diodes were fabricated using different n^+ layer conditions as the sole variable—was conducted with a fixed total thickness for all devices. Using *EQE* as the primary parameter for determining diode performance, it was determined that varying the n^+

layer deposition power had different effects on the *EQE* of these diodes based on the photon energy of incident light. Increasing the n^+ layer deposition power increased the doping concentration but also increased the defect density of the n^+ layer. For high energy light, the increased doping concentration manifested itself as increased V_{OC} and improved *EQE*. For low energy light, the increased defect density resulted in greater parasitic light absorption, which manifested itself as lower optical transmittance and reduced *EQE*.

The third and final experiment explored the effect of light illumination direction on the *EQE* of PIN diodes, as well as the extent to which the inclusion of a metallic reflector layer affected diode performance. It was determined that bottom illumination, i.e. illumination through the p^+ layer, significantly improved the *EQE* of the diodes under blue and green light because their higher energy photons experience a lesser degree of parasitic absorption when passing through *p*-type a-Si:H as opposed to *n*-type a-Si:H. Additionally, holes—which have a much lower carrier lifetime than electrons—need not travel as far as electrons due to the lower penetration depth of higher energy photons. Under red light, which can pass through the entirety of the PIN tri-layer, bottom illumination slightly reduced the *EQE* of the diodes because, when passing through the p^+ layer first, red light generates more excitons near the *p*-type side, which requires that photogenerated electrons travel further through the *i* layer than the photogenerated holes do. Since recombination events are more likely for electrons due to the highly defective *i/n* interface, this effect is amplified when electrons and holes do not differ much in drift distance, as is the case for red light illumination. The inclusion of a metallic reflector

layer improved *EQE* for all diodes regardless of incident light color and illumination direction. This improvement was most pronounced under red light because red light transmits through a-Si:H more compared to other colors. Reflecting the light back through the tri-layer effectively doubles the available thickness of the diode for absorption and exciton generation, which increases the current generated by a given amount of light and, consequently, the *EQE*.

Through the experiments covered in this work, I gained a greater understanding of the physics of photovoltaics as well as the mechanics of photodiodes. Laboratory techniques such as PECVD, sputtering, photolithography, profilometry, and *J-V* analysis made the work of this thesis possible. I would once again like to thank my advisor, Dr. Yue Kuo, and my colleagues, Kibum Kim and Shumao Zhang, for their assistance and guidance.

6. REFERENCES

[1] A. Einstein, "On a Heuristic Point of View About the Creation and Conversion of Light," *Annalen der Physik,* vol. 17, no. 6, pp. 132-148, 1905.

[2] A. E. Becquerel, "Mémoire sur les effets électriques produits sous l'influence des rayons solaires," *Comptes Rendus,* vol. 9, pp. 561-567, 1839.

[3] U.S. Department of Energy, "The History of Solar," 2002. [Online]. Available: http://www1.eere.energy.gov/solar/pdfs/solar_timeline.pdf. [Accessed 2016].

[4] Federal Ministry for Economic Affairs and Energy, "Zeitreihen zur Entwicklung der erneuerbaren Energien in Deutschland," 2016. [Online]. Available: http://www.erneuerbare-energien.de/EE/Redaktion/DE/Downloads/zeitreihen-zur-entwicklung-der-erneuerbaren-energien-in-deutschland-1990-2015.pdf?__blob=publicationFile&v=6. [Accessed 2016].

[5] Electricity production from solar and wind in Germany in 2014, 5 January 2015. [Online]. Available: https://www.ise.fraunhofer.de/de/downloads/pdf-files/data-nivc-/stromproduktion-aus-solar-und-windenergie-2014.pdf. [Accessed 2016].

[6] Y. Kuo, Thin Film Transistors - Materials and Processes - Volume 1 - Amorphous Silicon Thin Film Transistors, New York, New York: Kluwer Academic Publishers, 2004.

[7] T. Thomson, A System of Chemistry in Four Volumes, 5th ed., London: Baldwin, Cradock, and Joy, 1817.

[8] M. E. Weeks, "The discovery of the elements XII. Other elements isolated with the aid of potassium and sodium: beryllium, boron, silicon, and aluminum," *J. Chem. Educ.*, vol. 9, no. 8, pp. 1386-1412, 1932.

[9] W. E. Spear and P. G. Le Comber, "Electronic properties of substitiutionally doped amorphous Si and Ge," *Phil. Mag.*, vol. 33, no. 6, pp. 935-949, 1976.

[10] T. Matsui, M. Tsukiji, H. Saika, T. Toyama and H. Okamoto, "Correlation between Microstructure and Photovoltaic Performance of Polycrystalline Silicon Thin Film Solar Cells," *Jpn. J. Appl. Phys.*, vol. 41, pp. 20-27, 2002.

[11] R. C. Chittick, J. H. Alexander and H. F. Sterling, "The Preparation and Properties of Amorphous Silicon," *J. Electrochem. Soc.*, vol. 116, no. 1, pp. 77-81, 1969.

[12] W. E. Spear and P. G. Le Comber, "Substitutional doping of amorphous silicon," *Solid State Commun.*, vol. 17, pp. 1193-1196, 1975.

[13] W. Schülke, "Structural investigation of hydrogenated amorphous silicon by X-ray diffraction," *Phil. Mag. B*, vol. 43, no. 3, pp. 451-468, 1981.

[14] A. V. Shah, H. Schade, M. Vanecek, J. Meier, E. Vallat-Sauvain, N. Wyrsch, U. Kroll, C. Droz and J. Bailat, "Thin-film Silicon Solar Cell Technology," *Prog. Photovolt.: Res. Appl.*, vol. 12, pp. 113-142, 2004.

[15] B. Rech and H. Wagner, "Potential of amorphous silicon for solar cells," *Appl. Phys. A*, vol. 69, pp. 155-167, 1999.

[16] M. Ristova, Y. Kuo and H. H. Lee, "Study of hydrogenated amorphous silicon thin films as a potential sensor for He-Ne laser light detection," *Appl. Surf. Sci.,* vol. 218, pp. 44-53, 2003.

[17] National Renewable Energy Laboratory, "Best Research-Cell Efficiencies," 2016. [Online]. Available: http://www.nrel.gov/ncpv/images/efficiency_chart.jpg. [Accessed 2016].

[18] R. A. Street, "Doping and the Fermi Energy in Amorphous Silicon," *Phys. Rev. Lett.,* vol. 49, no. 16, pp. 1187-1190, 1982.

[19] R. A. Street, J. Zesch and M. J. Thompson, "Effects of doping on transport and deep trapping in hydrogenated amorphous silicon," *Appl. Phys. Lett.,* vol. 43, pp. 672-674, 1983.

[20] A. Shah, Ed., Thin-film Silicon Solar Cells, 1st ed., Lausanne: EPFL Press, 2010.

[21] Y. Kuo, K. Okajima and M. Takeichi, "Plasma processing in the fabrication of amorphous silicon thin-film-transistor arrays," *IBM J. Res. Develop.,* vol. 43, no. 1/2, pp. 73-88, 1999.

[22] G. Ganguly and A. Matsuda, "Defect formation during growth of hydrogenated amorphous silicon," *Phys. Rev. B,* vol. 47, no. 7, pp. 3661-3670, 1993.

[23] J. Nelson, The Physics of Solar Cells, 1st ed., London: Imperial College Press, 2003.

[24] A. Richter, M. Hermle and S. W. Glunz, "Reassessment of the Limiting Efficiency for Crystalline Silicon Solar Cells," *IEEE J. Photovolt.*, vol. 3, no. 4, pp. 1184-1191, 2013.

[25] SunPower, "SunPower Announces New World Record Solar Cell Efficiency," PR Newswire, New York, 2010.

[26] D. E. Carlson and C. R. Wronski, "Amorphous silicon solar cell," *Appl. Phys. Lett.*, vol. 28, pp. 671-673, 1976.

[27] M. I. Kabir, S. A. Shahamadi, V. Lim, S. Zaidi, K. Sopian and N. Amin, "Amorphous Silicon Single-Junction Thin-Film Solar Cell Exceeding 10% Efficiency by Design Optimization," *Int. J. Photoenergy,* vol. 2012, 2012.

[28] F. A. Rubinelli, "The origin of quantum efficiencies greater than unity in a-Si:H Schottky barriers," *J. Appl. Phys.*, vol. 75, no. 2, pp. 998-1004, 1994.

[29] K. Henry and Y. Kuo, "Effect of n+ Layer Deposition Power on Light Sensing of PIN Amorphous Silicon Diodes," *Electrochem. Soc. Trans.*, vol. 72, 2016.

[30] H. Miki, S. Kawamoto, T. Maejima, H. Sakamoto, M. Hayama and Y. Onishi, "Large Scale and Large Area Amorphous Silicon Thin Film Transistor Arrays for Active Matrix Liquid Crystal Displays," *Mat. Res. Soc. Symp. Proc.*, vol. 95, pp. 431-436, 1987.

[31] Y. Y. Ong, B. T. Chen, F. E. H. Tay and C. Iliescu, "Process Analysis and Optimization on PECVD Amorphous Silicon on Glass Substrate," *J. Phys.: Conf. Ser.*, vol. 34, pp. 812-817, 2006.

[32] W. S. Yan, S. Xu, C. C. Sern, T. M. Ong and H. P. Zhou, "RF power dependence of the properties of n-type nanocrystalline silicon films deposited by a low-frequency inductively coupled plasma," *J. Phys. D: Appl. Phys.,* vol. 44, pp. 455304-455309, 2011.

[33] M. Rusop, H. Ebisu, M. Adachi, T. Soga and T. Jimbo, "Physical and Microstructural Properties of Radio-Frequency Plasma-Enhanced Chemical Vapor Deposition Grown n-Type Phosphorus Doped Amorphous Carbon Films on the Contribution to Carbon-Based Solar Cells," *Jpn. J. Appl. Phys.,* vol. 44, no. 8, pp. 6124-6130, 2005.

[34] W. Son, Y. Moon, S. Lee and S. Choi, "Effects of RF Power and Substrate Temperature on the Performance of Thin-Film Silicon Solar Cells," *Mol. Cryst. and Liq. Cryst.,* vol. 602, pp. 200-206, 2014.

[35] J. Ding, F. Ye, S. Wang and N. Yuan, "Effects of phosphorus-doping on the microstructures, optical and electric properties in n-type Si:H thin films," *Key Eng. Mater.,* vol. 483, pp. 711-715, 2011.

[36] P. C. Mathur, J. Inderbir and R. M. Mehra, "Physics of Device Grade Amorphous Silicon," *Mater. Sci. Forum,* Vols. 223-224, pp. 221-228, 1996.

[37] S. M. de Nicolás, D. Muñoz, A. S. Ozanne, N. Nguyen and P. J. Ribeyron, "Optimisation of doped amorphous silicon layers applied to heterojunction solar cells.," *Energy Procedia,* vol. 8, pp. 226-231, 2011.

[38] T. Sameshima, N. Andoh and Y. Andoh, "Activation Behavior of Boron and Phosphorus Atoms Implanted in Polycrystalline Silicon Films by Heat Treatment at 250°C," *Jpn. J. Appl. Phys.*, vol. 44, no. 3, pp. 1186-1191, 2005.

[39] I. Ulber, R. Saleh, W. Fuhs and H. Mell, "Recombination at defects in amorphous silicon (a-Si:H)," *J. Non-Cryst. Solids,* vol. 190, pp. 9-20, 1995.

[40] A. M. Johnson, D. H. Auston, P. R. Smith, J. C. Bean, J. P. Harbison and A. C. Adams, "Picosecond transient photocurrents in amorphous silicon," *Phys. Rev. B,* vol. 23, no. 12, pp. 6816-6819, 1981.

[41] K. Baert, J. Vanhellemont, W. Vendervorst, J. Nijs and M. Konagai, "Heavily phosphorus-doped epitaxial Si deposited by low-temperature plasma-enhanced chemical vapor deposition," *Appl. Phys. Lett.*, vol. 59, no. 7, pp. 797-789, 1991.

[42] L. Fadila, B. Abdelkader, S. Jamaldine, B. Yahia, C. Larbi and A. Ana, "Density of states in Intrinsic and n/p-Doped Hydrogenated Amorphous and Microcrystalline Silicon," *J. Mod. Phys.*, vol. 2, pp. 1030-1039, 2011.

[43] S. S. Hegedus and W. N. Shafarman, "Thin-Film Solar Cells: Device Measurements and Analysis," *Prog. Photovolt.: Res. Appl.,* vol. 12, pp. 155-176, 2004.

[44] National Renewable Energy Laboratory, "Air Mass 1.5," January 2003. [Online]. Available: http://rredc.nrel.gov/solar/spectra/am1.5/. [Accessed 2016].

[45] C. A. Gueymard, "The sun's total and spectral irradiance for solar energy applications and solar radiation models.," *Solar Energy,* vol. 76, no. 4, pp. 423-453, April 2004.

[46] P. Y. Yu and M. Cardona, Fundamentals of Semiconductors: Physics and Materials Properties, 4th ed., Heidelberg: Springer, 2010.

[47] P. Mialhe, J. P. Charles, A. Khoury and G. Bordure, "The diode quality factor of solar cells under illumination," *J. Phys. D: Appl. Phys.*, vol. 19, pp. 483-492, 1986.

[48] S. Morawiec, M. J. Mendes, S. A. Filonovich, T. Mateus, S. Mirabella, H. Águas, I. Ferreira, F. Simone, E. Fortunato, R. Martins, F. Priolo and I. Crupi, "Broadband photocurrent enhancement in a-Si:H solar cells with plasmonic back reflectors," *Opt. Express*, vol. 22, no. S4, pp. A1059-A1070, 2014.

[49] T. Tiedje, E. Yablondovitch, G. D. Cody and B. G. Brooks, "Limiting Efficiency of Silicon Solar Cells," *IEEE Trans. Electron. Dev.*, Vols. ED-31, no. 5, pp. 711-716, 1984.

[50] V. Jovanov, J. Ivanchev and D. Knipp, "Standing wave Spectrometer," *Opt. Express*, vol. 18, no. 2, pp. 426-438, 2009.

[51] J. Zhu, C. Hsu, Z. Yu, S. Fan and Y. Cui, "Nanodome Solar Cells with Efficient Light Management and Self-Cleaning," *Nano Lett.*, vol. 10, pp. 1979-1984, 2010.

[52] K. F. Brennan, Introduction to Semiconductor Devices, 1st ed., Cambridge University Press, 2005.

[53] H. Wieczorek, "Effects of Trapping in a-Si:H Diodes," *Solid State Phenom.*, Vols. 44-46, pp. 957-972, 1995.

APPENDIX A: PLOT OF SPECTRAL IRRADIANCE OF AM 1.5 SOLAR LIGHT

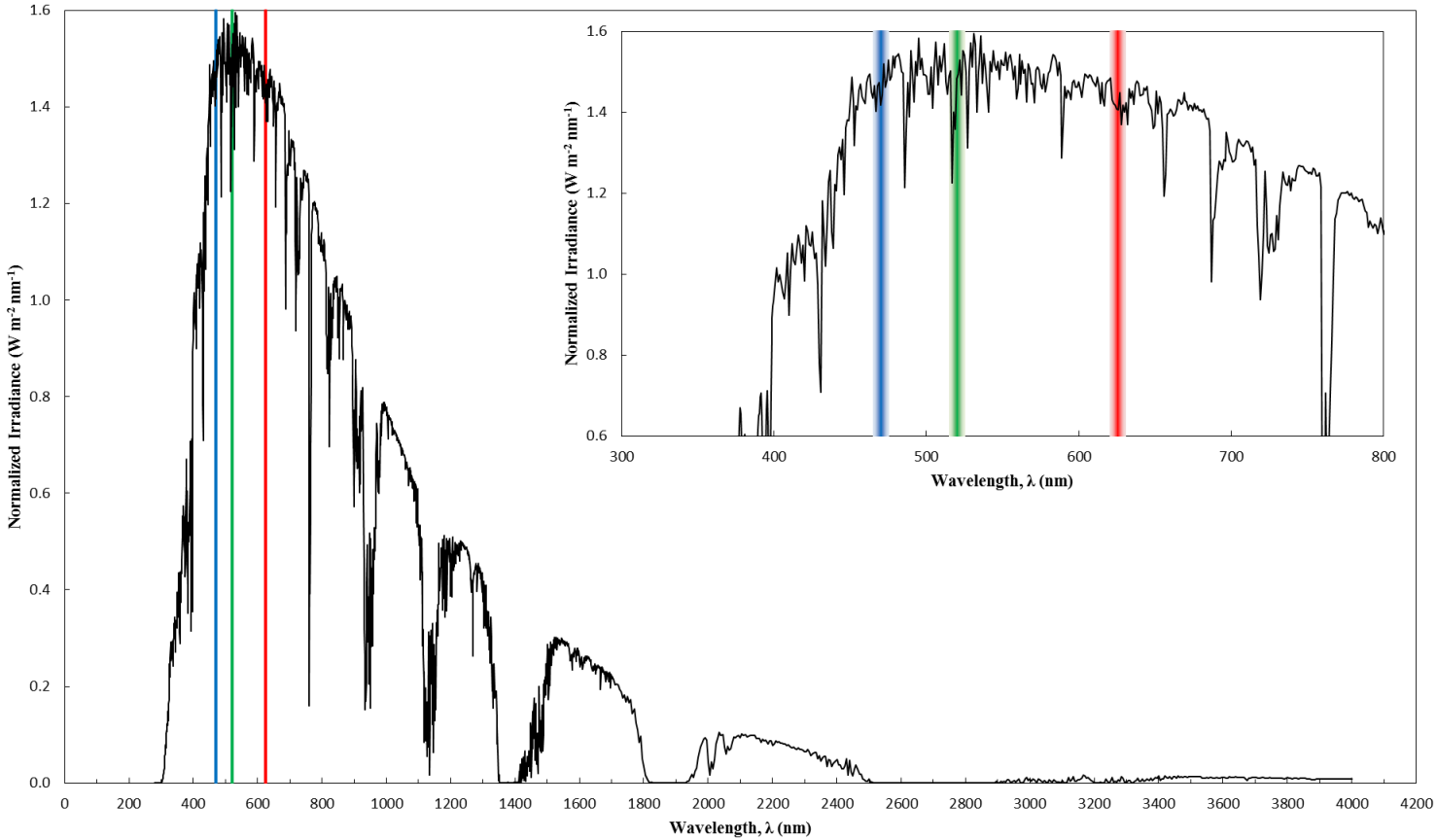

Figure A-1: Spectral irradiance of AM 1.5 solar light vs. light wavelength normalized to a total intensity of 1000 W/m^2. Red, green, and blue lines indicate the spectral irradiance and wavelength of their corresponding photons. Inset shows detail of the visible light spectrum

APPENDIX B: PLOTS OF ALL OPTICAL CHARACTERISTICS FOR EXPERIMENT 2

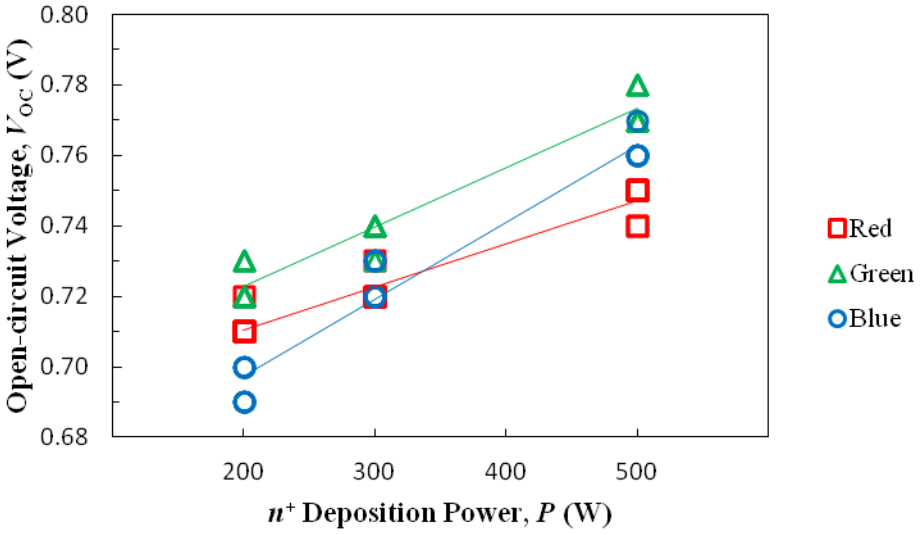

Figure B-1: V_{OC} vs. n^+ deposition power under red, green, and blue light.

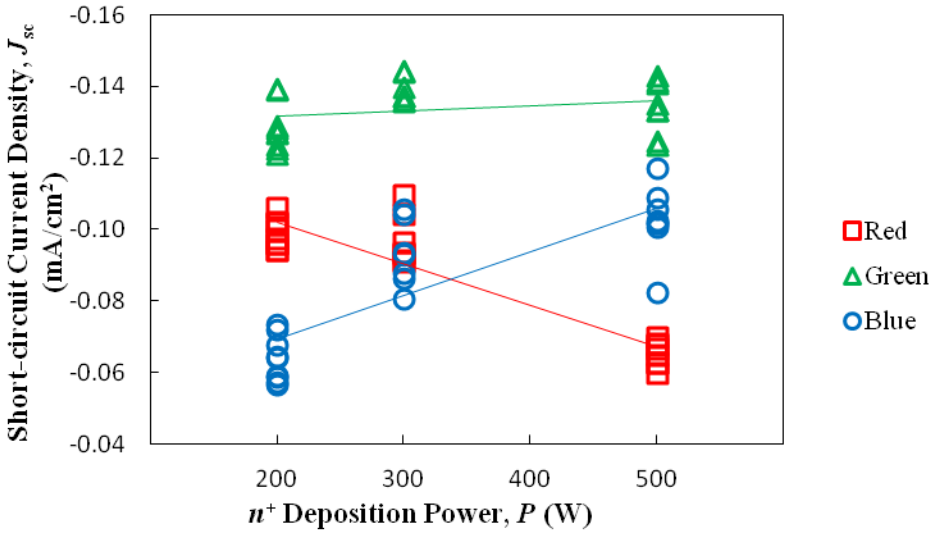

Figure B-2: J_{SC} vs. n^+ deposition power under red, green, and blue light.

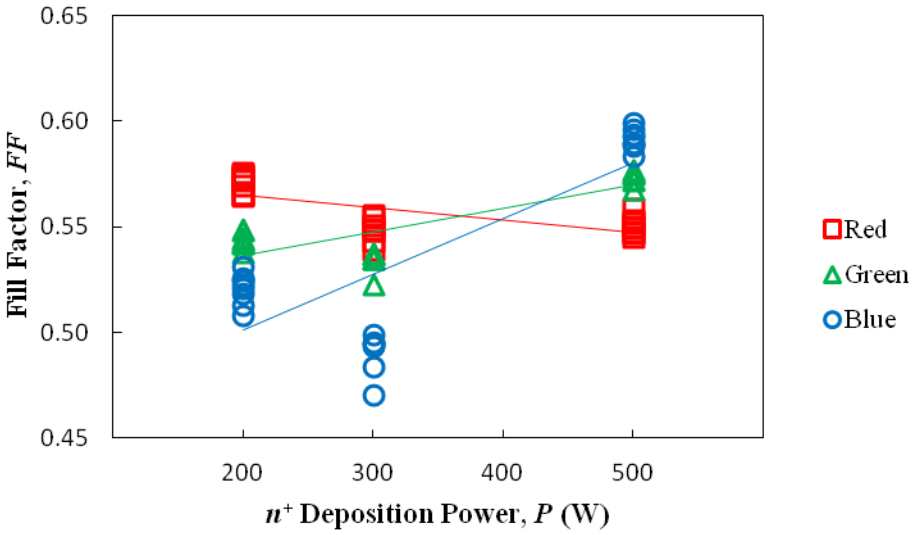

Figure B-3: *FF* vs. n^+ deposition power under red, green, and blue light.

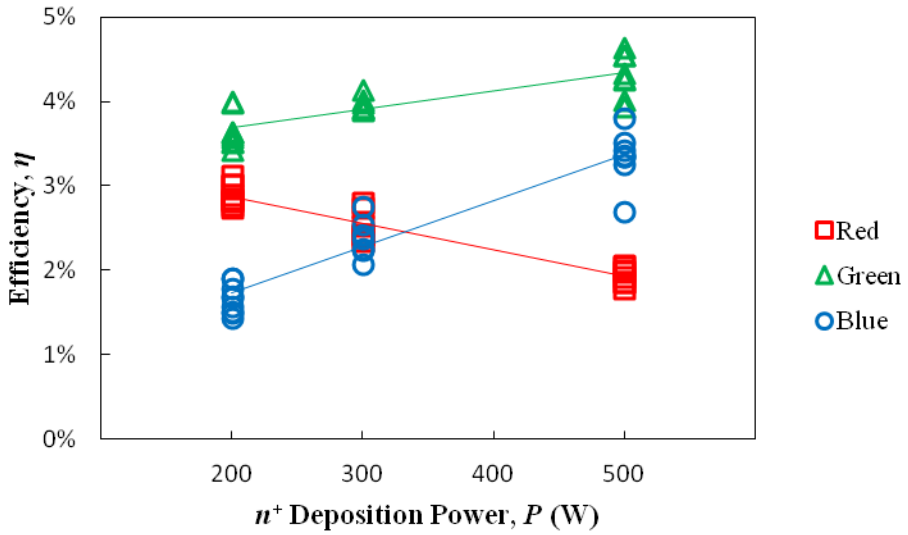

Figure B-4: η vs. n^+ deposition power under red, green, and blue light.

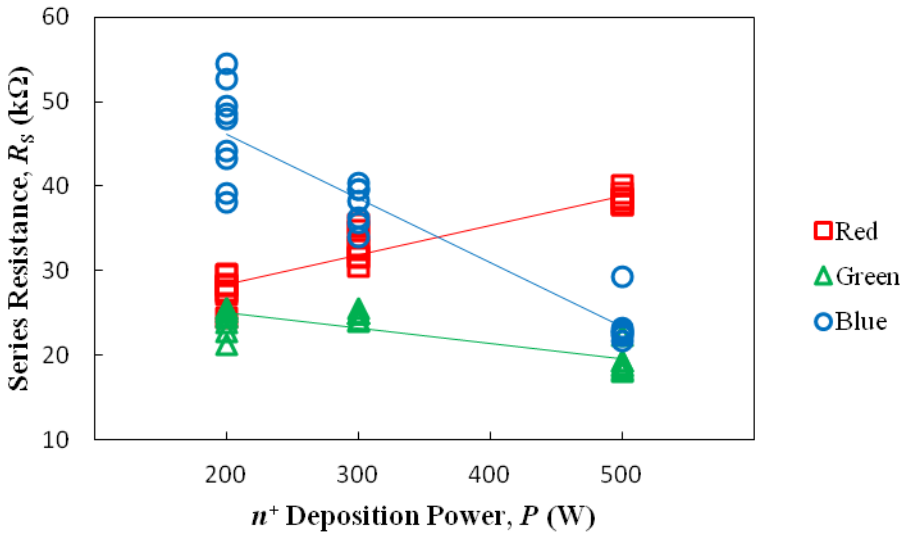

Figure B-5: R_S vs. n^+ deposition power under red, green, and blue light.

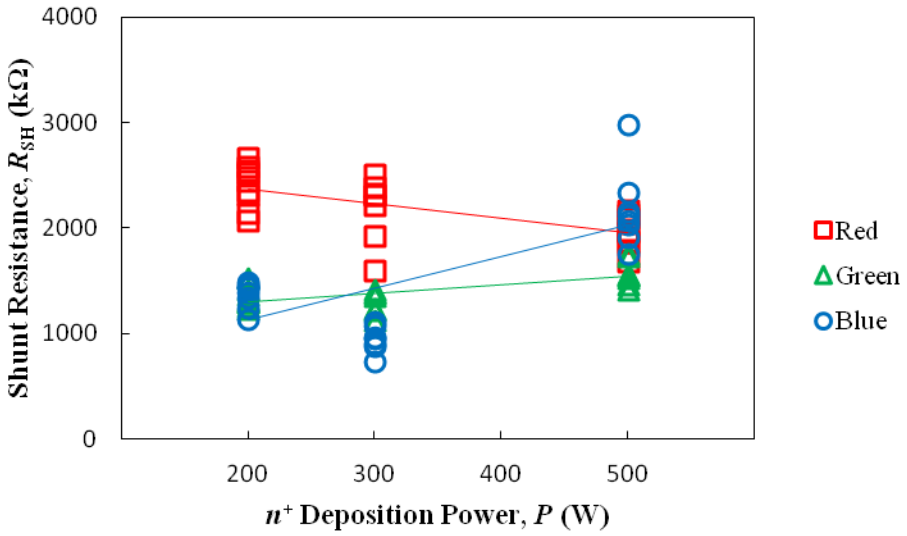

Figure B-6: R_{SH} vs. n^+ deposition power under red, green, and blue light.

APPENDIX C: PLOTS OF ALL OPTICAL CHARACTERISTICS FOR EXPERIMENT 3

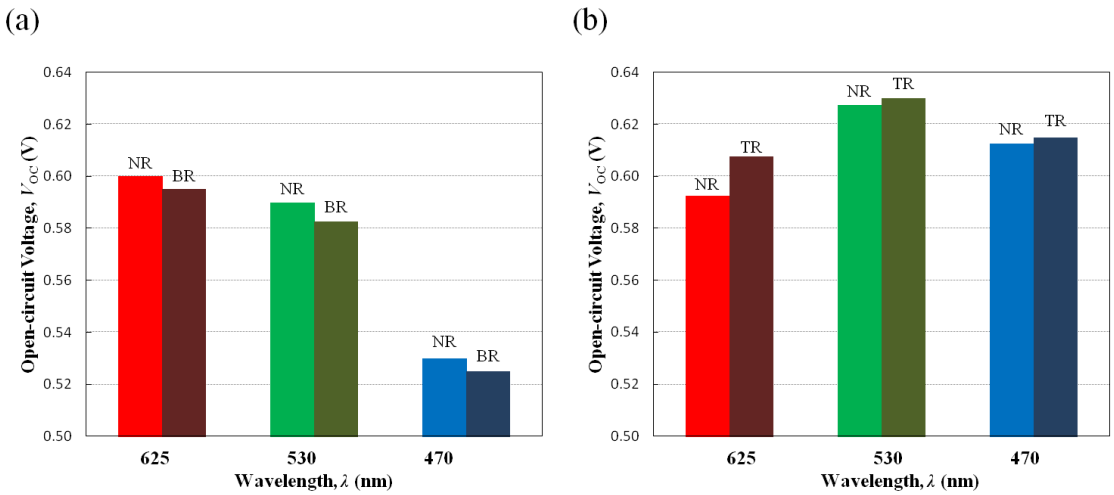

Figure C-1: V_{OC} vs. incident light wavelength, with and without back reflectors, when under (a) top illumination and (b) bottom illumination. Precision of data resulted in error bars that would not have been visible.

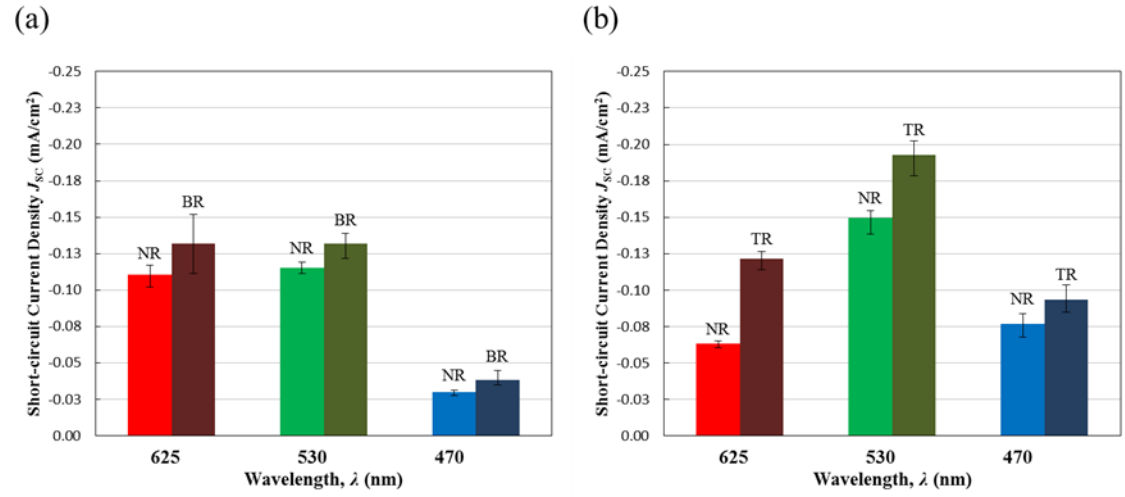

Figure C-2: J_{SC} vs. incident light wavelength, with and without back reflectors, when under (a) top illumination and (b) bottom illumination. Error bars indicate full range of data for each condition.

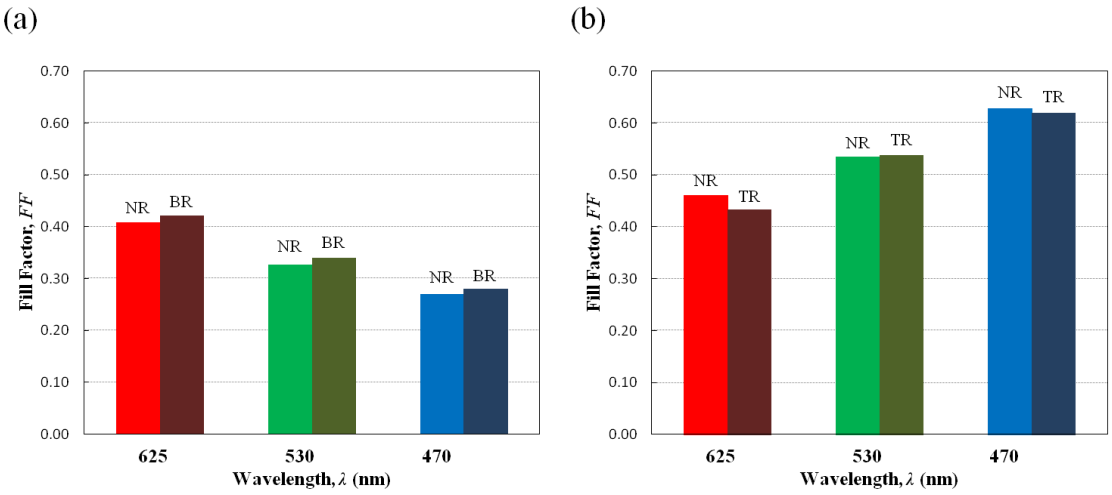

Figure C-3: *FF* vs. incident light wavelength, with and without back reflectors, when under (a) top illumination and (b) bottom illumination. Precision of data resulted in error bars that would not have been visible.

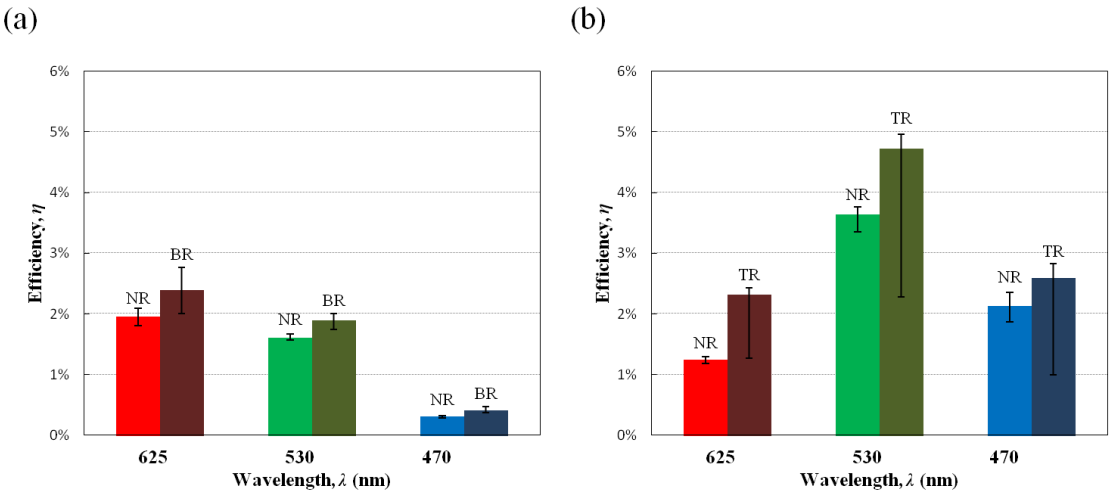

Figure C-4: η vs. incident light wavelength, with and without back reflectors, when under (a) top illumination and (b) bottom illumination. Error bars indicate full range of data for each condition.

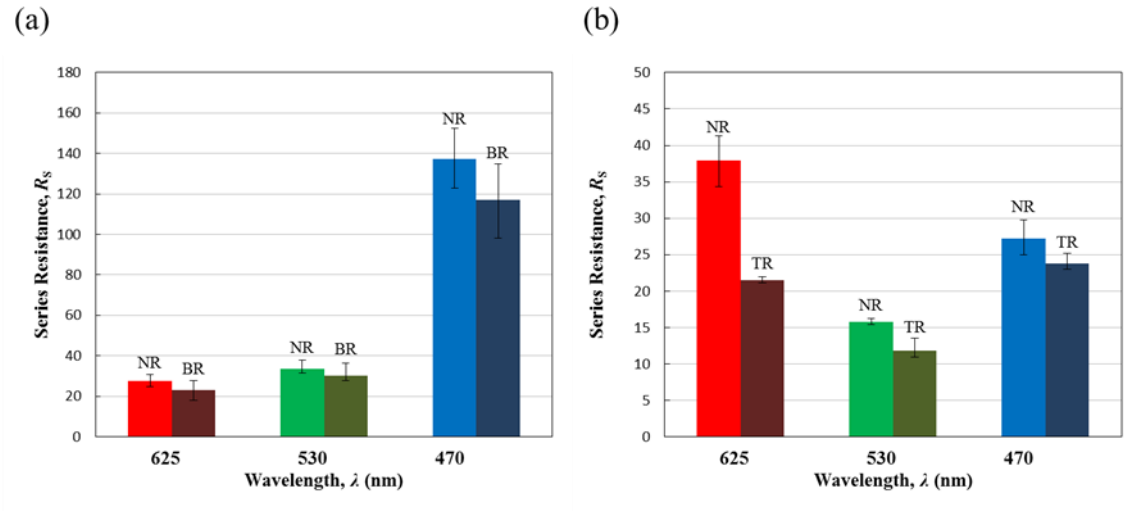

Figure C-5: R_S vs. incident light wavelength, with and without back reflectors, when under (a) top illumination and (b) bottom illumination. Error bars indicate full range of data for each condition.

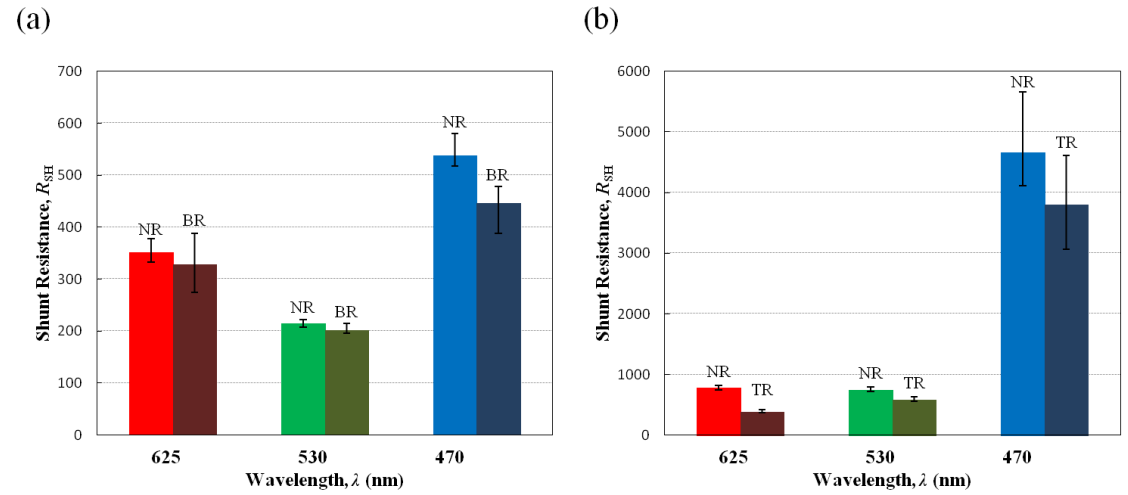

Figure C-6: R_{SH} vs. incident light wavelength, with and without back reflectors, when under (a) top illumination and (b) bottom illumination. Error bars indicate full range of data for each condition.